UNIVERSITY OF CAMBRIDGE

Department of Engineering

Aerodynamic design of helium turbines for rocket engines

Author Name: William Davis

Supervisor: Dr Chris Clark

Date: 27/05/2020

.

Aerodynamic Design of Helium Turbines for Rocket Engines

William Davis

Gonville & Caius College

Supervisor: Dr Chris Clark

Department of Engineering
University of Cambridge

May 2020

Declaration
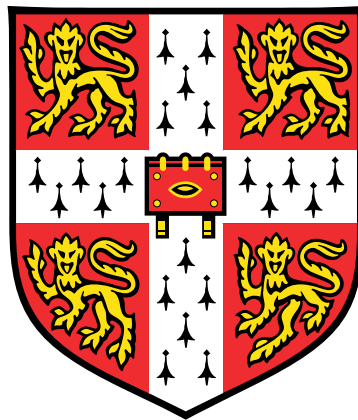
I hereby declare that, except where specifically indicated, the work submitted herein is my own original work.

Signed: _____   Date: __27/05/2020__

Acknowledgements

Abstract

SABRE is a precooled combined cycle engine for single-stage-to-orbit spaceplanes. Air entering the engine is cooled by an air-to-helium heat exchanger and the helium is used in a turbine to drive an air compressor. Constraints imposed on the helium turbine by the precooler, compressor and gas properties force it into an unconventional design space. Previous work has shown that shroud and trailing edge losses dominate as a result, with up to forty stage designs suggested for high efficiency. This project focuses on the aerodynamic design of the helium turbine, with the aim of reducing the number of stages needed to achieve adequate efficiency.

Aerodynamic modelling is undertaken, using loss correlations to estimate efficiency, and an optimisation routine is used to find designs for maximum efficiency. Interrogation of chosen designs reveals that shroud loss dominates across the design space. The optimal design point therefore mitigates leakage as far as possible, utilising low flow coefficients, stage loading and aspect ratios to increase blade spans and balance profile, trailing edge and secondary losses. The optimal design point shifts as the number of stages increases in response to reductions in shroud and trailing edge losses.

The optimal ten stage helium turbine design is compared to a representative aeroengine HP turbine. It is shown that the HP turbine operates at a 40 % lower radius and 5–10 times larger blade spans as a result of differences in the working gases and design constraints. When these constraints are relaxed and the HP turbine is optimised for aerodynamic performance it better resembles the optimal helium turbine design.

Blade geometry in the turbine is limited by machining tolerances, vibration control and aerodynamic limits. A sensitivity study shows that halving the shroud gap or utilising an enhanced stator shroud could reduce the required number of stages needed for 85 % efficiency from nineteen to twelve. A further halving of the trailing edge thickness and an increase in pitch-to-chord ratio to 1.5 using high lift blades pushes this down to seven stages, demonstrating the possibilities for high efficiency and low mechanical complexity.

Thermomechanical modelling is undertaken to predict turbine mass and transient expansion that will cause the shroud gap to change during operation. Results show that designs with fewer stages require thicker hubs to withstand increased centrifugal stress. This results in an increase in mass, suggesting that designs with more stages benefit from being lightweight as well as more efficient. An analysis of the change in the shroud gap during start-up reveals transient expansions as much as 90 % of the blade span. Use of a thicker casing can mitigate the effect; in depth mechanical design may consider tapered discs and blades to better control expansion.

Contents

List of Figures

List of Tables

1 Introduction

This project investigates challenges associated with aerodynamic design of the helium turbine in Reaction Engines' SABRE, a combined cycle rocket engine capable of air breathing flight at speeds of up to Mach 5. Turbine design and loss modelling is undertaken to find dominant loss mechanisms and resulting turbine geometry. Thermomechanical problems associated with stress and transient expansion are also considered to show how they may further constrain design. This project has been run alongside another which has investigated the rotordynamic behaviour and machinability of designs, with findings from each project informing the investigations of the other.

1.1 Reaction Engines and SABRE

The Synergetic Air-Breathing Rocket Engine (SABRE) under development by Reaction Engines Limited (REL) is a precooled combined cycle engine intended for use on a reusable single-stage-to-orbit (SSTO) spaceplane. SABRE is capable of operating in both air-breathing and pure rocket modes. In air-breathing mode atmospheric air is used as the oxidiser, but at speeds beyond Mach 5 the intake closes and SABRE becomes a conventional rocket engine, using stored liquid oxygen to burn the hydrogen fuel and accelerate into orbit. This dual mode operation allows for significant savings on the mass of stored oxygen, reducing the overall fuel burn [1]. Scimitar, a purely air-breathing derivative of SABRE, has also been considered for the LAPCAT A2, a hypersonic transport aircraft concept [2].
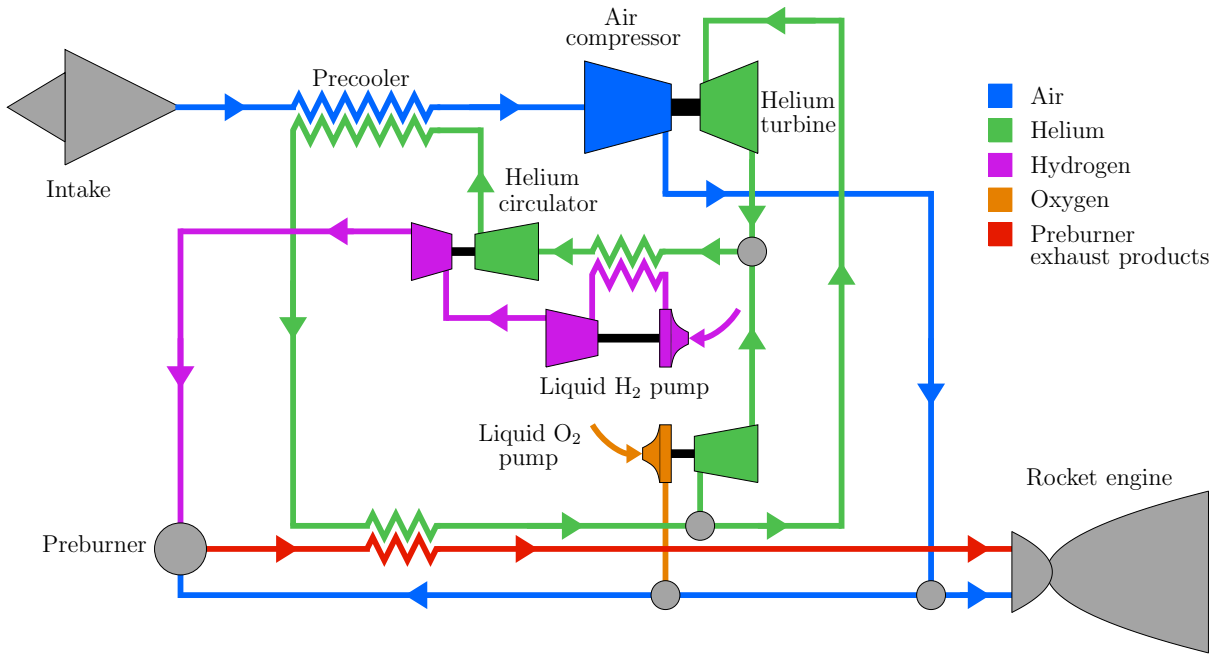
Figure 1: Simplified SABRE cycle

Figure 1 shows a simplified representation of SABRE. At Mach 5 the ram-compression of air entering the engine means it reaches temperatures in excess of 1250 K. To allow for further compression without the need for high temperature materials the air is brought down to 125 K with a precooler [3]. The design of a lightweight, high performance heat exchanger [4] has been the main technical challenge since the engine's inception in the 1980s as part of the HOTOL project [5], and as such the rest of the engine is constrained by precooler design. After cooling the air passes through a turbo-compressor and enters the combustion chamber to be burnt with hydrogen.

This project focuses on the helium turbine, seen coupled to the air compressor in Fig.1. The constraints on the turbine, provided by REL, are listed in table 1. Each constraint arises as a result of the turbine's connection to the rest of the cycle. Mass flow rate and inlet pressure and temperature are limited by the helium loop, which is designed around the requirements of the precooler. This is the limiting piece of technology, so all other components must be designed to match it. The power requirement and rotational speed are set by the air compressor. At present REL have elected to use a pre-existing compressor design, meaning the turbine must be designed to match its power requirement. To avoid the mechanical complexity and mass of a high performance gearbox the turbine is directly coupled to the compressor, so the speeds are also matched.

Turbine constraints		
$P_{0,in}$	145	bar
$T_{0,in}$	950	K
$\dot{W}$	17	MW
$\dot{m}$	16	$\mathrm{kg\,s^{-1}}$
Ω	6782	rpm

Table 1: Turbine constraints

The combined cycle used in SABRE will be sensitive to the conditions in each individual loop. Zhang et al. [6] showed that cycle efficiency could be increased by 3 % and specific impulse by 8.3 % with a higher helium temperature at inlet and a lower mass flow rate, but did not consider how this would affect turbine efficiency. Fernández-Villacé & Paniagua [7] simulated SABRE using performance maps for the turbomachinery and demonstrated that there is significant scope for optimisation of each component to achieve greater whole engine efficiency. The work in this project therefore seeks to improve SABRE through improved design of the helium turbine.

1.2   Helium turbines

The thermophysical properties of helium gas, given in table 2, are significantly different to those of air or hydrocarbon combustion products, resulting in equally different turbo-machinery geometries. These properties lead to several different behaviours. At the same temperature, the speed of sound in helium is three times that in air, leading to low Mach number machines. To extract the same amount of work the temperature drop needed is five times lower in helium at the same mass flow rate, leading to a lower pressure ratio. For example, the pressure ratio of the helium turbine in SABRE is only two, compared to a pressure ratio of 150 [3] for the air compressor.

Helium properties [8]		
γ	1.6625	
c_p	5187	$\mathrm{J\,kg^{-1}\,K^{-1}}$
R	2067	$\mathrm{J\,kg^{-1}\,K^{-1}}$

Table 2: Gas properties

Helium turbines have found potential applications in nuclear power, where they have been considered for use in high-temperature gas-cooled reactors. These turbines have similar constraints to those imposed in SABRE, particularly with the rotational speed which must match the synchronous speed of the generator. Large scale turbines have been built for demonstrator reactors that operate at high pressures and low pressure ratios, using as many as twenty stages and hub-to-tip ratios over 0.9 [9]. Van den Braembussche et al. [10] undertook a design study on such a turbine, demonstrating that the very low Mach numbers found in helium facilitate simplified design of a multi-stage turbine.

Previous work on helium turbine design for SABRE has focused on the use of counter-rotating turbines to achieve a compact design. A numerical study by Paniagua et al. [11] demonstrated the feasibility of such a turbine when coupled to a twin-shaft air compressor, suggesting efficiencies over 90 % for a four-rotor-row design operating at much higher speeds and mass flow rates than those in table 1. Waldren et al. [12] showed that although counter-rotating turbines can be considered to be similar to conventional turbines by using relative non-dimensional parameters, a counter-rotating design will be more efficient due to differences in spanwise velocity distributions.

Low order studies conducted so far for complete turbine design have shown the need for many stages to achieve adequate efficiency for the SABRE helium turbine. Desai [13] undertook loss modelling and suggested designs of up to forty stages would be required to overcome problems associated with shroud leakage and trailing edge losses. Clark [14] verified these findings with CFD, considering both conventional and counter-rotating designs. The author worked on a UROP [15] to reconstruct Desai's modelling, focusing

on designs with repeating stages and investigating the effect of trailing edge thickness in a CFD study. Results confirmed Desai's conclusions on the need for many stages but suggested lower efficiencies than those found previously.

The conclusions of all previous work have suggested that to achieve high efficiency for the SABRE helium turbine a mechanically complex design utilising many stages and counter-rotation is necessary. In order to reduce the complexity, and thus both mass and cost, REL are seeking a non-counter-rotating design with an acceptable efficiency of 85 % and as few stages as possible. This is the key aim of this project.

1.3 Aerodynamic and mechanical design

Preliminary design of the helium turbine begins with choosing a turbine architecture through scaling. Assuming 85 % efficiency to find turbine exit density, the specific speed can be calculated as

$$\Omega_s = \left(\frac{\dot{m}}{\rho_{out}}\right)^{\frac{1}{2}} \Omega(\Delta h_0)^{-\frac{3}{4}} = \left(\frac{16}{4.75}\right)^{\frac{1}{2}} \times \frac{6782 \times 2\pi}{60} \times \left(\frac{17 \times 10^6}{16}\right)^{-\frac{3}{4}} = 0.04 \quad (1)$$

where the definition of specific speed is for compressible flow machines [16]. Comparing this value to Csanady's [17] chart matching specific speed to machine type suggests that a Pelton wheel would be best for this low specific speed. There are, however, problems with such a choice. Consider a single stage Pelton wheel with zero absolute tangential velocity at rotor exit ($V_{\theta 3} = 0$) and a radius of 0.5 m, representative of suggested designs for SABRE. The required absolute tangential velocity at inlet to the rotor $V_{\theta 2}$ can be found with the Euler work equation like so

$$\Delta h_0 = \frac{\dot{W}}{\dot{m}} = U_2 V_{\theta 2} = r_2 \Omega V_{\theta 2} \quad (2)$$

$$V_{\theta 2} = \frac{\dot{W}}{\dot{m} r_2 \Omega} = \frac{17 \times 10^6 \times 60}{16 \times 0.5 \times 6782 \times 2\pi} = 2992 \,\mathrm{m\,s^{-1}} \quad (3)$$

Using this in the Mach number relation [18]

$$\frac{V_{\theta 2}}{\sqrt{c_p T_{02}}} = \frac{2992}{\sqrt{5187 \times 950}} = \sqrt{\gamma - 1} M_{\theta 2} \left(1 + \frac{\gamma - 1}{2} M_{\theta 2}^2\right)^{-\frac{1}{2}} \quad (4)$$

gives the absolute tangential Mach number at rotor inlet as 5.47. Even without including any radial component of velocity this is far too high for a realistic machine. Although large Pelton wheels used in hydraulic applications can be highly efficient, small scale versions

with a gas as the working fluid perform much worse. They are used in dental drills with efficiencies around 20 % [19], requiring significant cooling [16], and have been suggested for use in refrigeration with efficiencies around 30 % [20]. Wood [21] suggests that at very low specific speeds axial gas turbines become preferable for maximum efficiency. An axial design is therefore sought in this project.

A characteristic of low specific speed machines is high hub-to-tip ratios, over 0.9. Figure 2 shows the scale of a turbine with a hub-to-tip ratio of 0.97, representative of designs seen in this project. The reason for this is the mismatch between power output, rotational speed and volumetric flow rate. The fixed work requirement and rotational speed necessarily sets the radius while the combination of low mass flow rate and high gas density set the low volumetric flow rate, resulting in a thin annulus with small blade spans.
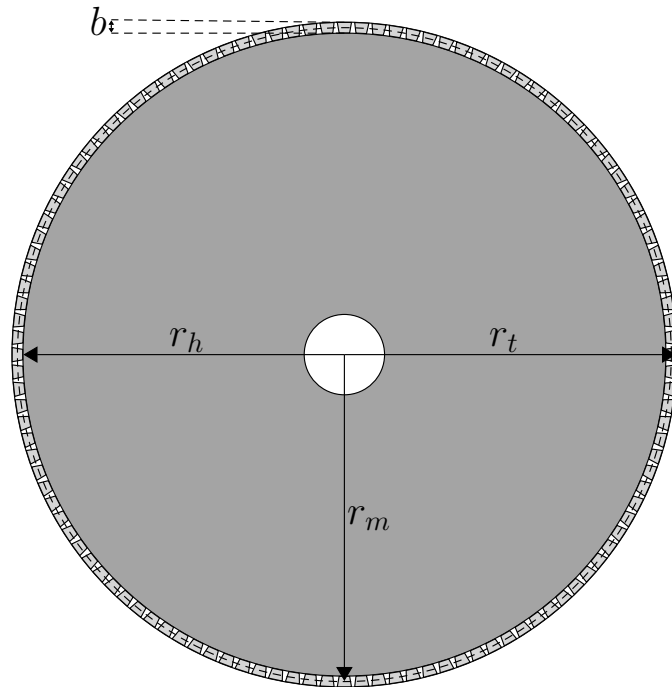
Figure 2: Axial view of a turbine disc with $r_h/r_t = 0.97$

The consequence of small blade spans, with correspondingly small chords, is that geometric constraints become significant. Trailing edge thickness and shroud gap are set by mechanical limits in machining capability and vibration control, so they become large fractions of blade chord and height respectively. As found by both Desai [13] and Davis [15] this results in trailing edge and shroud loss dominating, driving the designer towards low radius multi-stage designs that allow larger blades. Karimjee's project on aeromechanical design looks to address these mechanical constraints, investigating blade machining and rotordynamics. For the purposes of this project both trailing edge thickness and shroud gap have been set at 0.3 mm, representative of current capabilities of in-house trailing edge machining and a recognised achievable shroud gap.

1.4 Research questions

1. What are the key loss mechanisms and geometric constraints in the helium turbine and how should design change to reach the efficiency required in SABRE?

2. How does the design of the helium turbine compare to that seen in modern aero-engines?

3. How sensitive is the helium turbine to changes in the geometric constraints imposed on it by vibration, machining and aerodynamic design limitations?

4. How does transient thermomechanical behaviour change the geometric constraints on the turbine?

1.5 Turbine conventions

Throughout this report angles and velocities are defined as positive in the direction of rotation, with angles measured from the axial direction consistent with Denton's convention [22]. This is summarised in Fig.3(a). Where necessary, referenced equations are adjusted from their source in order to match this convention. Figure 3(b) shows the geometry of a turbine blade row, with relevant parameters labelled as they will be used throughout.

(a)   (b)
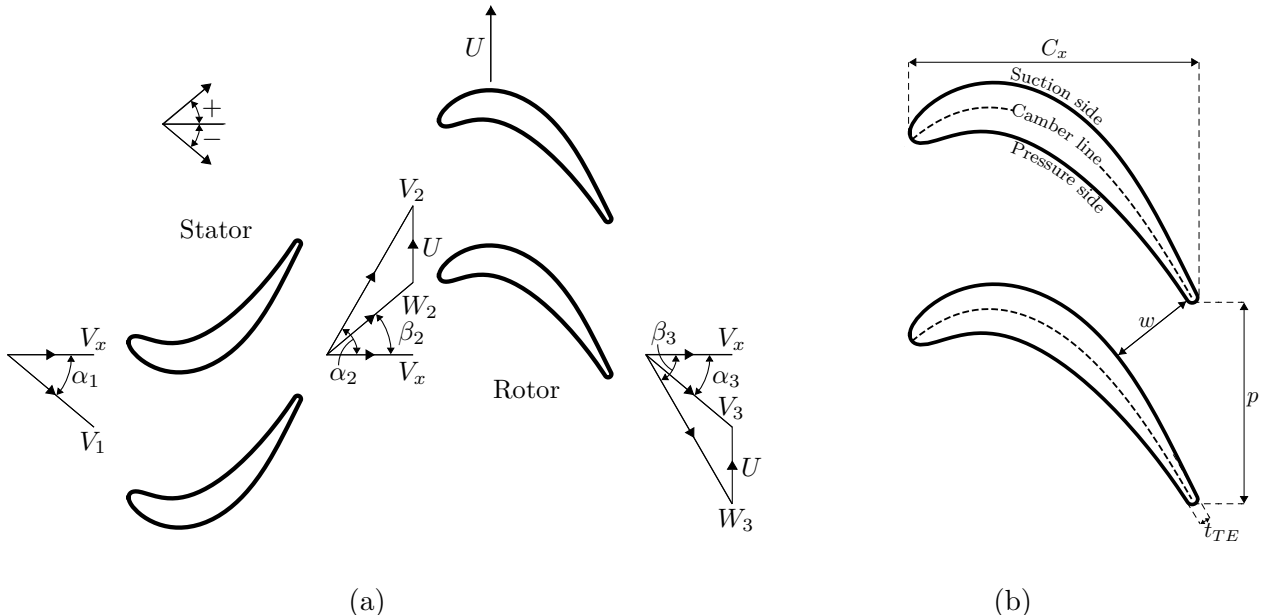
Figure 3: Turbine stage and blade geometry convention

2 Aerodynamic Design

Aerodynamic design of the helium turbine for SABRE looks to generate geometries and estimate efficiency. Correlations are used to predict the entropy production by different physical mechanisms and show how they are affected by design parameters, which then allows for designs to be optimised for maximum efficiency. This section will describe the approach taken for aerodynamic modelling and how results influence design choices.

2.1 Modelling approach

Previous work on this turbine has limited the degrees of freedom in its design by using repeating stages at a constant radius [13] [15]. There is, however, no need for this to be the case and optimal designs often have non-repeating stages that vary in radius [23]. This opens up many more degrees of freedom, up to the point where each parameter can be set for each individual stage. For the purposes of this project the parameters of the first and last stages are set as inputs to the model with the rest of the stages determined using a linear variation. Allowing each stage to vary independently would result in as many as a hundred floating variables for a twenty stage machine, compared to only ten when specifying just the stages at each end. This reduces the complexity of optimisation and means machines with different numbers of stages can be compared with greater ease. It is physically reasonable to assume that changes through a multi-stage machine will be smooth and in a single direction due to the continued expansion, and early tests using more control points with higher order splines indicated that this is the case.

The model has been written using Python 3, an interpreted high-level language for scientific computing. As inputs it takes the design constraints, listed in table 1, the constraints on trailing edge thickness and shroud gap, $t_{TE} = g = 0.3\,\mathrm{mm}$, the number of stages in the turbine n and the parameters for the first and last stages. These stage parameters are flow coefficient ϕ, stage loading coefficient ψ, reaction Λ, blade aspect ratio AR and the ratio of enthalpy change over the first and last stages $\Delta h_{0,n}/\Delta h_{0,1}$, which requires only one number to define it for the whole turbine. Each of $n, \phi, \psi, \Lambda, \Delta h_{0,n}/\Delta h_{0,1}$ and AR are floating variables in design.

With inputs specified, geometry can be found for each stage. The model is a mean-line analysis so mean radius, taken to be constant across a stage, is found from from the definition of stage loading coefficient as

$$r_m = \sqrt{\frac{\Delta h_0}{\psi \Omega^2}} \tag{5}$$

Although Δh_0 varies from stage to stage, to a first approximation it can be thought of as

7

as the total enthalpy change over the turbine divided by the number of stages, $\dot{W}/\dot{m}n$. This inverse relationship implies that doubling the number of stages will reduce the radius by a fraction of $\sqrt{2}$. Midspan blade speed is therefore

$$U = \Omega r_m \tag{6}$$

and so axial velocity, also taken as constant through the stage, is given by

$$V_x = U\phi \tag{7}$$

Continuity of mass flow through a blade row sets blade span as

$$b = \frac{\dot{m}}{2\pi r_m \rho V_x} \tag{8}$$

and using the defined aspect ratio the blade axial chord follows

$$C_x = \frac{b}{\text{AR}} \tag{9}$$

All major dimensions have now been set; all that is left are the flow angles for each stage and the throat width. For a repeating stage, where inlet flow angle and velocity are assumed to be equal to those at the exit, the angles are fully defined by ϕ, ψ and Λ. For the non-repeating stages used here the assumption of the inlet matching the exit is removed, so one more variable must be fixed to define the stage. To do this the inlet flow of the first stage is set to be axial i.e. a swirl angle of zero. From there all of the angles for the first stage can be found and, using the constraint that the inlet angle for a stator must match the absolute exit angle of the preceding rotor ($\alpha_{1,i+1} = \alpha_{3,i}$), the angles for every stage can be found with their specified ϕ, ψ and Λ. The absolute exit angle from the rotor is given by

$$\alpha_3 = \tan^{-1}\left(\frac{-2\psi + \sqrt{4\psi^2 - 4\Lambda(2\psi\Lambda - \phi^2\Lambda\tan^2\alpha_1 - 2\psi + \psi^2)}}{2\phi\Lambda}\right) \tag{10}$$

and using this the exit angle from the stator is

$$\alpha_2 = \tan^{-1}\left(\tan\alpha_3 + \frac{\psi}{\phi}\right) \tag{11}$$

These are different to the usual equations for repeating stages given in turbomachinery textbooks such as Saravanamuttoo et al. [24]. A full derivation is given in appendix A.1.

The relative flow angles needed for the rotor follow as

$$\beta_2 = \tan^{-1}\left(\tan\alpha_2 - \frac{1}{\phi}\right) \tag{12}$$

$$\beta_3 = \tan^{-1}\left(\tan\alpha_3 - \frac{1}{\phi}\right) \tag{13}$$

To find the throat width for a blade row a pitch-to-chord ratio p/C_x is needed. Zweifel's criterion [25] is often used for this based on minimum profile loss, but designs found in this project often have blades with high swirl angles and low angular deflection, resulting in unrealistically large blade spacing when using Zweifel's rule. p/C_x is therefore set to be within the normal range of 0.75–1.5 for turbines [23], $p/C_x = 1.1$ unless stated otherwise. With the spacing set the throat width is given by

$$w = p\cos\alpha_2 = C_x\left(\frac{p}{C_x}\right)\cos\alpha_2 \tag{14}$$

Turbine geometry is now set, however Eq.8 shows that blade height, and thus chord from Eq.9, depends on gas density, which in turn depends on pressure through the ideal gas law. Pressure depends not only on enthalpy extraction but also entropy generation, which depends on blade height and chord, and so an iterative scheme is needed to match them. The stagnation pressure at exit from a blade row can be found by combining the definition of stagnation pressure loss coefficient for a turbine [22]

$$Y_p = \frac{P_{01} - P_{02}}{P_{02} - P_2} \tag{15}$$

with the perfect gas relation for compressible flow [18]

$$P_2 = P_{02}\left(1 + \frac{\gamma - 1}{2}M_2^2\right)^{-\frac{\gamma}{\gamma-1}} \tag{16}$$

like so

$$Y_p(P_{02} - P_2) = P_{01} - P_{02} \tag{17a}$$

$$P_{02}\left[Y_p + 1 - \left(1 + \frac{\gamma - 1}{2}M_2^2\right)^{-\frac{\gamma}{\gamma-1}}\right] = P_{01} \tag{17b}$$

$$P_{02} = \frac{P_{01}}{Y_p + 1 - Y_p\left(1 + \frac{\gamma-1}{2}M_2^2\right)^{-\frac{\gamma}{\gamma-1}}} \tag{17c}$$

The compressible flow relation is used in Eq.16 even though, due to the high speed of sound in helium, Mach numbers in the turbine are low enough to consider the flow incompressible. As it requires no knowledge of density, as an incompressible relation would, it can be used along with the ideal gas law in a calculation to find density and avoid an extra iteration. An initial guess of $Y_p = 5\%$ is used in the first instance, and the subsequent loss calculated can be used to find a new loss coefficient. This process is repeated until Y_p has converged, usually within three iterations.

Loss is calculated using correlations for profile loss due to blade surface boundary layers, trailing edge loss due to the finite trailing edge thickness and mixing of the wake, shroud loss due to leakage flow over the blade shroud and secondary loss due to secondary flows. These mechanisms are visualised in Fig.4. The equations that follow seek to capture the key physics of each mechanism and reflect how they are affected by design changes.
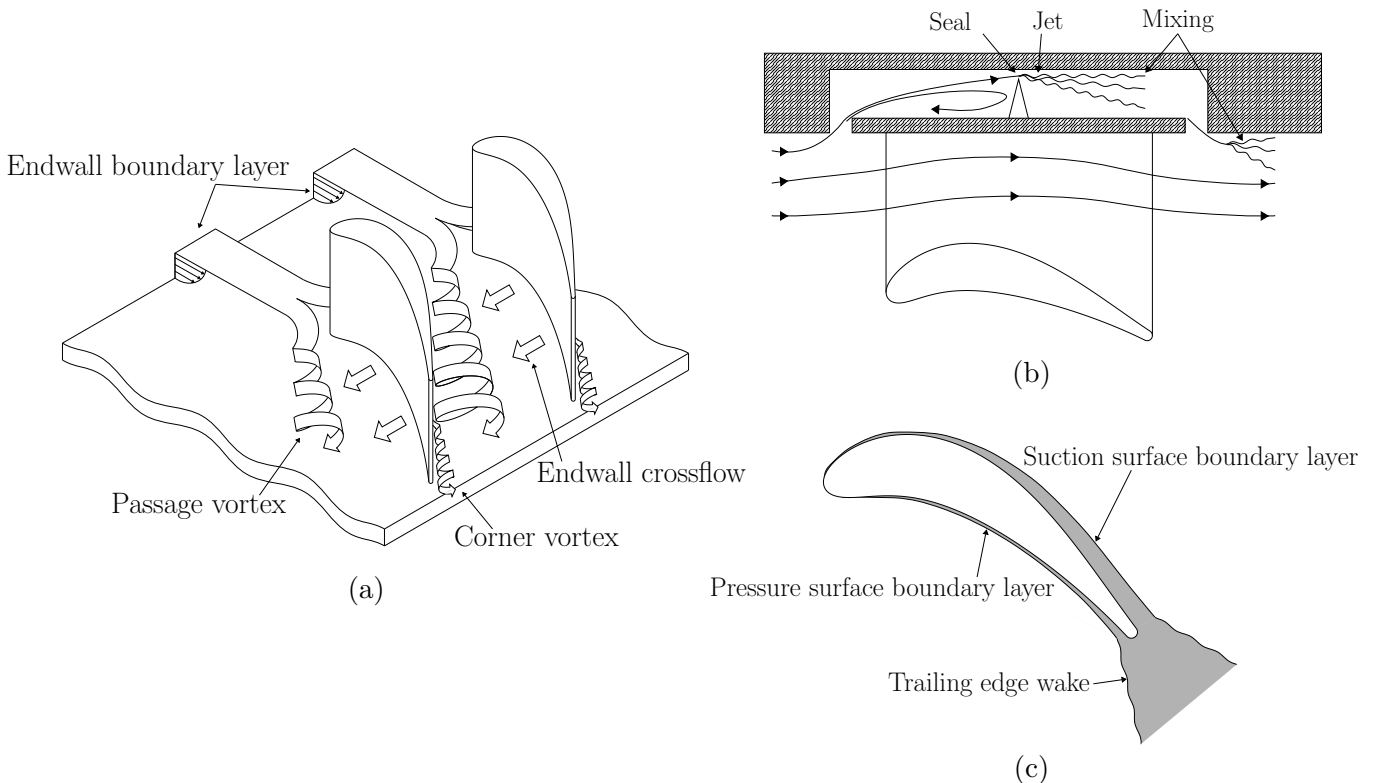
Figure 4: Visualisations of (a) secondary flows (b) shroud leakage (c) profile boundary layers and the trailing edge wake

In this project only shrouded blades are considered. In previous work all designs are found to have small blade spans of 5 mm–25 mm, meaning the fixed shroud gap of 0.3 mm is 1 %–6 % of the total blade height. Yoon et al. [26] showed that shrouded blades are more efficient above a certain break-even clearance, which varies depending on design but is less than 1 %. This is demonstrated in Fig.5 from Yoon et al. [26], showing a break-even clearance of 0.58 % of blade span. Between zero and break-even clearance the unshrouded turbine is more efficient due to additional losses in the shroud cavity, which causes the

offset loss at zero clearance, but designs considered here operate outside of this regime and so unshrouded blades are neglected.
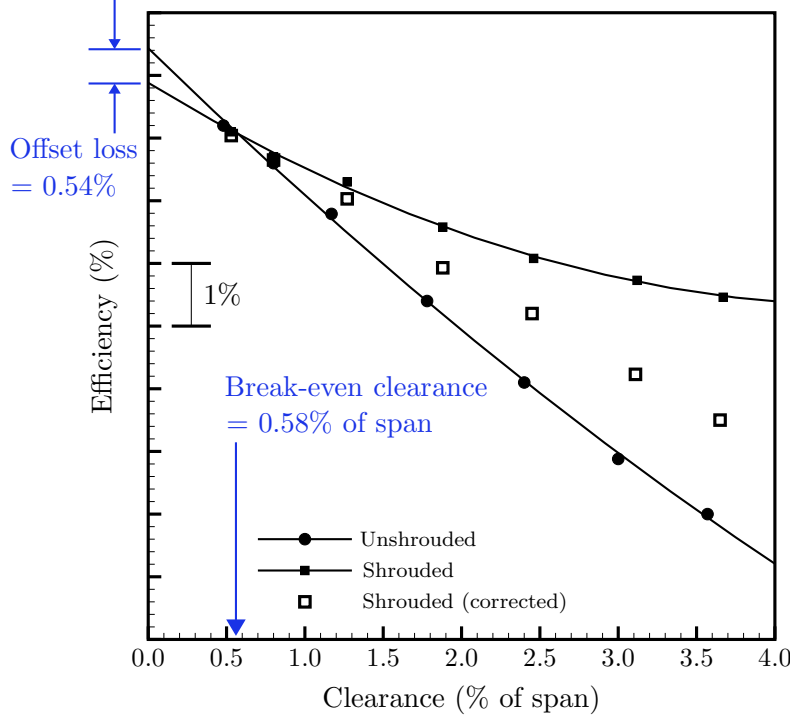
Figure 5: Effect of clearance on shrouded and unshrouded turbines with $50\,\%$ reaction [26]

Denton's [22] equation for shroud leakage loss considers the leakage flow as a fraction of the main flow, which depends on the clearance as a fraction of the span and the turning over the blade. A contraction coefficient C_c is used to reflect shroud design [27] and a typical value of 0.6 suggested by Denton will be used here. The leakage fraction is

$$\frac{m_L}{m_m} = \frac{gC_c}{b}\sqrt{\sec^2 \alpha_2 - \tan^2 \alpha_1} \tag{18}$$

and the resulting entropy rise from leakage is

$$\Delta s_{shr} = \frac{m_L}{m_m}\frac{V_2^2}{T_2}\left(1 - \frac{\tan \alpha_1}{\tan \alpha_2}\sin^2 \alpha_2\right) \tag{19}$$

Profile loss arises as a result of dissipation in the boundary layers on the blade surfaces. This is dominated by the thicker, lossier boundary layer on the suction surface. Vázquez et al. [28] showed that this affect can be best captured by using a Reynolds number based on the length of the suction surface l_{ss} like so

$$Re = \frac{\rho_2 V_2 l_{ss}}{\mu_2} \tag{20}$$

11

The model calculates l_{ss} by generating blade profiles from axial chord and inlet and exit angles. Bézier curves define the turning distribution and Kulfan's [29] class function/shape function transformation method is used for the shape space thickness distribution. The dynamic viscosity of helium depends on its temperature, so Petersen's correlation [30] is used to calculate it as

$$\mu = 3.674 \times 10^{-7} \times T^{0.7} \tag{21}$$

This correlation aligns well with with data from Arp et al. [8]. This Reynolds number is used to calculate the blade surface dissipation coefficient using a variation of Schlichting's model [31], giving

$$C_{d,pro} = 0.002 \left(\frac{Re}{500\,000} \right)^{-0.2} \tag{22}$$

Denton's [22] equation for the profile entropy loss coefficient uses the fractional change in velocity on the blade surface $\Delta V / \bar{V}$, assumed to be the optimal value of $1/\sqrt{3}$, giving

$$\zeta_{s,pro} = C_{d,pro} \left(2\frac{\bar{V}}{\Delta V} + 6\frac{\Delta V}{\bar{V}} \right) |\tan \alpha_2 - \tan \alpha_1| \tag{23}$$

Due to the shroud leakage some of the flow doesn't experience dissipation from the blade profile. This is accounted for by using the leakage fraction from Eq.18, giving the entropy rise due to profile loss as

$$\Delta s_{pro} = \frac{\frac{1}{2}V_2^2}{T_2} \zeta_{s,pro} \left(1 - \frac{m_L}{m_m} \right) \tag{24}$$

To find loss due to the trailing edge, Denton [22] uses both the momentum and displacement boundary layer thicknesses. To calculate these it is assumed that the term $2\theta/w = \zeta_{s,pro}$ as given by Eq.23. Taking a shape factor $H = 1.4$ for a turbulent boundary layer, the displacement thickness is

$$\delta^* = H\theta = \frac{Hw\zeta_{s,pro}}{2} \tag{25}$$

Assuming the base pressure coefficient $C_{pb} = -0.15$ the trailing edge entropy loss coefficient is

$$\zeta_{s,TE} = \left(\frac{t_{TE} + \delta^*}{w} \right)^2 - \frac{C_{pb}t_{TE}}{w} \tag{26}$$

The first term in this equation represents the blockage from the boundary layer at the trailing edge and mixing of the wake while the second term represents form drag. Again, as the leakage flow doesn't pass over the trailing edge, the entropy rise due to the wake is

$$\Delta s_{TE} = \frac{\frac{1}{2}V_2^2}{T_2}\zeta_{s,TE}\left(1 - \frac{m_L}{m_m}\right) \tag{27}$$

Secondary loss is calculated using Dunham and Came's [32] correlation, a modification of the Ainley-Mathieson method [33]. Compared to the Ainley-Mathieson correlation, Dunham and Came's was shown to be particularly effective on low aspect ratio designs in which secondary flows take up a large portion of the blade passage. It is therefore suited to this model as designs often have low aspect ratios of unity or less. The equation requires the vector mean flow angle, defined as

$$\alpha_m = \tan^{-1}\left(\frac{\tan\alpha_1 + \tan\alpha_2}{2}\right) \tag{28}$$

Dunham and Came's equation was adjusted by Denton [34] to better fit experimental data, giving the stagnation pressure loss coefficient as

$$Y_{p,sec} = 0.375 \times 0.1336\frac{C_x}{b}\frac{\cos^3\alpha_2}{\sqrt{\cos\alpha_1}}\frac{(\tan\alpha_1 - \tan\alpha_2)^2}{\cos\alpha_m} \tag{29}$$

As the low Mach numbers found in designs mean flow can be considered incompressible, the stagnation pressure loss coefficient is considered to be identical to the entropy loss coefficient. This can be proved by considering the fundamental thermodynamic relation

$$T_0 ds = dh_0 - \frac{dP_0}{\rho} \tag{30}$$

With no work extraction from a perfect gas, $dh_0 = 0$ and $T_0 = T_{02}$. Dividing by $\frac{1}{2}V_2^2$ then gives

$$\frac{T_{02}ds}{\frac{1}{2}V_2^2} = -\frac{dP_0}{\frac{1}{2}\rho V_2^2} \tag{31}$$

Integrating both sides between blade row inlet and exit gives

$$\frac{T_{02}(s_2 - s_1)}{\frac{1}{2}V_2^2} = \frac{(P_{01} - P_{02})}{\frac{1}{2}\rho V_2^2} \tag{32}$$

For incompressible flow $T_{02} \approx T_2$ and $\frac{1}{2}\rho V_2^2 \approx P_{02} - P_2$, so Eq.32 states that $\zeta_s = Y_p$. The entropy rise from secondary loss is therefore

$$\Delta s_{sec} = \frac{\frac{1}{2}V_2^2}{T_2}Y_{p,sec} \tag{33}$$

The same reasoning can be used in reverse to find an overall stagnation pressure loss coefficient for the blade row

$$Y_{p,BR} = \frac{(\Delta s_{shr} + \Delta s_{pro} + \Delta s_{TE} + \Delta s_{sec})\,T_2}{\frac{1}{2}V_2^2} \tag{34}$$

This value us used in Eq.17c to match loss and geometry. Equations 14–34 use angles and flow properties for a stator, however they are identical for a rotor when correct relative values are used. After applying this methodology to every stage, the overall entropy rise across the turbine is found by summing each loss mechanism for each blade row

$$\Delta s = \sum_{\mathrm{BR}=1}^{2n} (\Delta s_{shr} + \Delta s_{pro} + \Delta s_{TE} + \Delta s_{sec}) \tag{35}$$

Entropy rise is converted to a lost work by multiplying by the exit stagnation temperature $T_{0,out}$, and this is used to find the total-to-total isentropic efficiency for the turbine as

$$\eta = \frac{\Delta h_0}{\Delta h_0 + T_{0,out}\Delta s} \tag{36}$$

Using the method described, the model can take in a set of constraints and design parameters to produce a complete turbine geometry and predict efficiency, which can be used as a cost function in optimisation. It has been packaged up into a graphical user interface, shown in Fig.6, which uses blade profiles generated to calculate l_{ss} for blade-to-blade visualisation. This allows for rapid testing of new designs using sliders to vary parameters. Outputs are shown on the right of Fig.6, including a maximum angle. A limit of 73° is placed on the blade exit angles to ensure machinability and model validity.

2.2 Design point optimisation

Finding an optimal design point requires a reliable optimisation routine that can be performed fast enough to be useful. Desai [13] and Davis' [15] previous work included brute force optimisation through testing a large set of possible parameters. This enabled examination of tradeoffs between different outputs, and both found Pareto efficient frontiers between turbine efficiency and volume. The problem with this approach is the time it
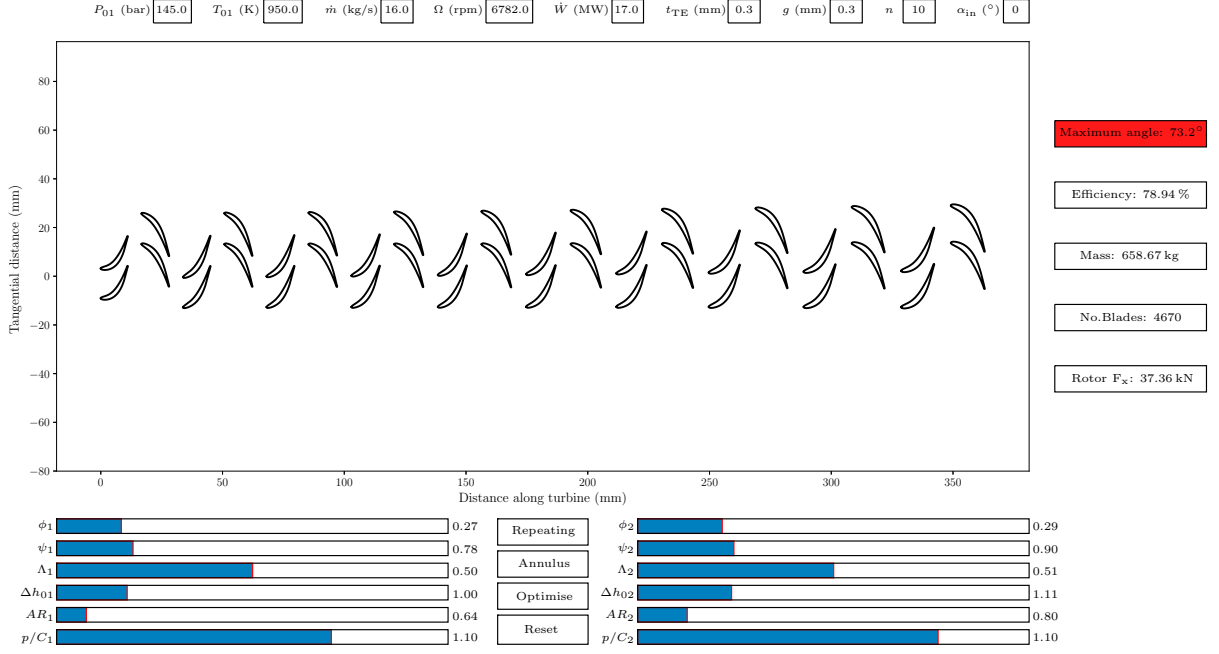
Figure 6: Turbine design graphical user interface

takes to test every member of the set of possible combinations of parameters, which is of the order of the number of options for each parameter to the power of the number of variables. When using repeating stages, where only five variables are needed, this set is quite small. This project however uses ten variables, five each for the first and last stages, making a brute force approach impractical.

There are many different options for efficient optimisation algorithms but not all are suited to this application. The problem is constrained by the limits on the variables, for example all of them must be positive and reaction must be between zero and one, so many algorithms cannot be used. Sequential least squares programming (SLSQP) [35] was chosen for its ease of use, being implemented in Python's SciPy library. SLSQP can handle the large number of variables and constraints, but it is susceptible to local minima and as such may not find the global optimum point. Table 3 shows the results from optimisation for efficiency using four different starting points. Points B and C reach the same end point, within the tolerances of the optimisation, but A and D have converged to different local optima as seen by the different efficiencies and end values for ϕ and ψ.

To avoid returning a local minimum the routine is run multiple times and the result with the highest efficiency is selected. 5000 starting points, selected using a coarse grid over the range of suitable values for each variable, are tested to ensure the full design space is covered. This is a significant reduction from the more than $2\,000\,000$ that would be needed to sufficiently resolve the space with a brute force method, and parallelising the calculation across several compute cores allows the points to be tested rapidly. Over $90\,\%$ of starting points converge to the global optimum, indicating the cost function is smooth

Design	Starting point			
parameter	**A**	**B**	**C**	**D**
ϕ	0.2	0.4	0.6	0.9
ψ	0.4	0.7	1.1	2.0
Λ	0.3	0.5	0.5	0.8
AR	0.5	0.8	1.2	2.0
$\Delta h_{0,n}/\Delta h_{0,1}$	0.5	1.0	1.2	2.0
	End point			
ϕ	0.23	0.28	0.29	0.35
ψ	0.51	0.84	0.84	1.53
Optimised efficiency (%)	77.12	78.92	78.88	77.73

Table 3: Comparison of optimisation results for a ten stage turbine using different starting points. Values for ϕ, ψ, Λ, AR are average values across the turbines

and well suited to this type of optimisation. A sensitivity analysis confirms this, showing a wide optimum with no sharp drops.

Results from optimisation are used to investigate loss sources and how changes to design affect them. The base design used for this is a ten stage turbine selected by the optimisation routine, for which parameters are listed in table 4.

Stage	ϕ	ψ	Λ	**AR**	$\frac{\Delta h_{0,n}}{\Delta h_{0,1}}$
1	0.27	0.78	0.50	0.64	1.11
10	0.29	0.90	0.51	0.80	

Table 4: Parameters for the first and last stages of the optimal ten stage design

Figure 7 shows specific lost work contributions from the models when varying ϕ, ψ AR and n for this design. In the figure the entropy rise from each mechanism has been non-dimensionalised by multiplying by exit stagnation temperature and normalising with total work output. From each of the graphs it is apparent that shroud loss is the dominant mechanism. As explained in section 1.3 this is a result of the high hub-to-tip ratios, and thus small blade spans, that lead from the constraints. Shroud loss makes up 60 % of total loss at the design point, whereas profile, trailing edge and secondary losses make up 15 %, 10 % and 15 % respectively. In a conventional gas turbine it would be expected that shroud, secondary and the combination of profile and trailing edge loss each produce about a third of total loss [22], however the relatively large shroud gap, 1 %–6 % of span compared to 1 %–2 % normally seen in turbines [36], means shroud loss dominates.

Figure 7(a) shows that reducing the flow coefficient reduces shroud loss. Equations 7 and 8 show that reducing ϕ will reduce axial velocity and thus increase blade spans, decreasing
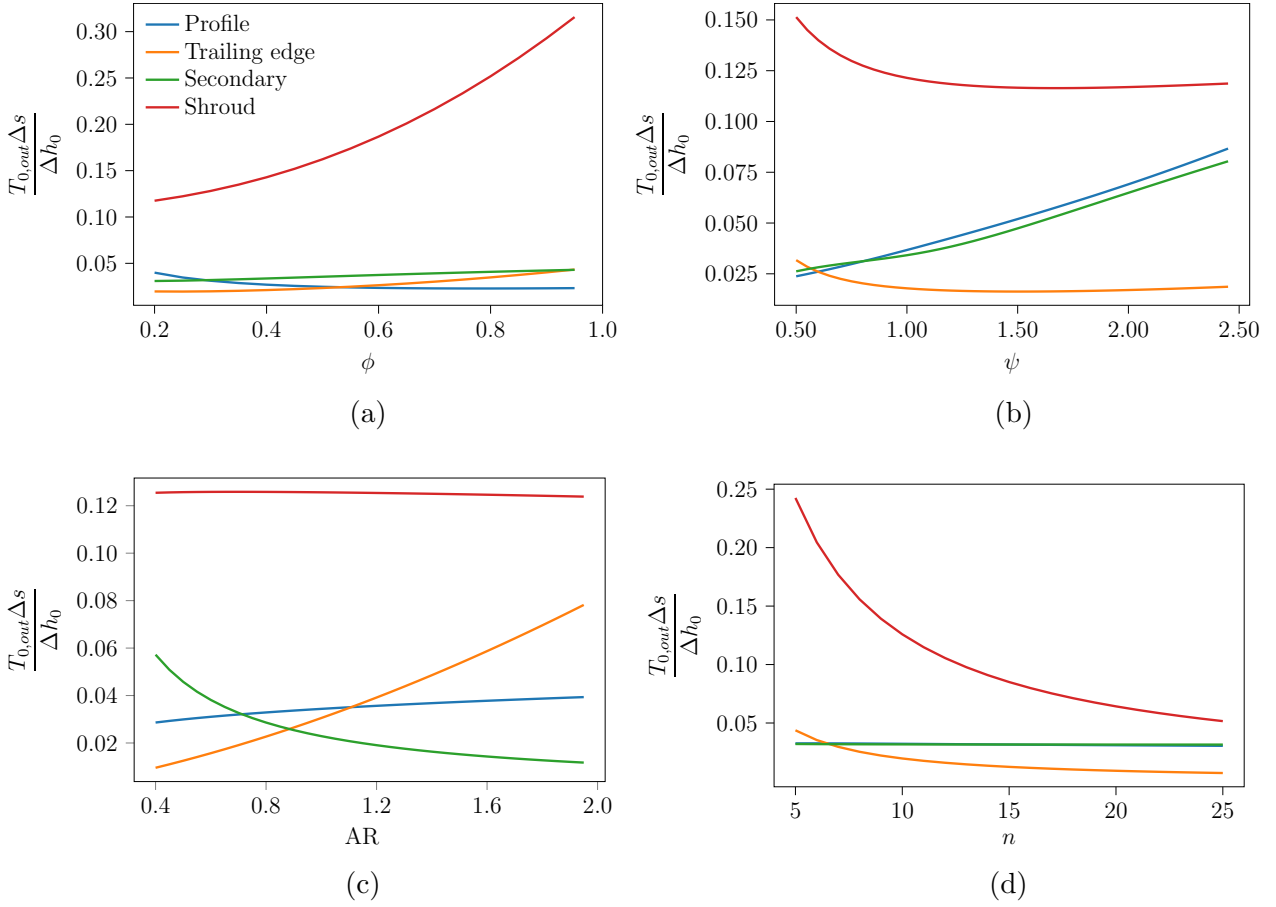
Figure 7: Normalised loss for each mechanism when varying (a) ϕ (b) ψ (c) AR (d) n. Constant parameters are set as in table 4 with $n = 10$

the effect of the shroud gap. This is limited at low ϕ by profile loss, which from Eq.23 increases due to the greater angular deflection that results from needing the same change in angular momentum in Euler's work equation but at a lower velocity. The resulting optimum lies around $\phi = 0.3$.

Equation 8 suggests that blade spans could be increased by reducing radius, which can be achieved by increasing the stage work coefficient. The problem with doing this is shown in Fig.7(b). The reduced radius only helps shroud loss to a certain point, beyond which it levels off. High ψ requires more flow turning, and combined with the low ϕ this results in deflections of over 120°. At values of ψ above 1.3 the terms depending on flow angle in Eqs.18 and 19, which represent the pressure difference over the blade and the mixing of the leakage jet with the main flow, penalise loss more than the decreasing radius helps. On top of this the increased turning over the blades increases both profile and secondary losses, so the optimum stage loading is around 0.8–0.9.

The effect of aspect ratio is to vary the axial chord for a given blade span, which is set by continuity of mass flow. A high aspect ratio will give relatively small chords, meaning the trailing edge thickness becomes a larger fraction of the chord, and by extension the

blade throat width through Eq.14. This fraction appears in both terms in Eq.26, showing that an increase in AR will be penalised strongly by trailing edge loss. On the other hand a low aspect ratio produces relatively large chords, resulting in the secondary flows taking up more of the blade passage and causing more dissipation. AR appears explicitly in Eq.29 to show that it is inversely proportional to secondary loss. Both of these effects are seen in Fig.7(c). The optimal AR balances the two mechanisms, leading to values of 0.6–0.8 that are lower than those usually seen in turbine design [24].

Previous studies [13] [15] have suggested designs with twenty or more stages to achieve high efficiency and this is supported by Fig.7(d). Increasing the number of stages reduces both shroud and trailing edge losses while leaving profile and secondary losses, which at this design point are equal, unchanged. More stages means less work per stage, bringing the mean radius down through Eq.5 and thus increasing blade spans and chords. As explained above this decreases shroud and trailing edge loss respectively, meaning total loss with twenty-five stages is just over a third of that with five stages.

The change in the relative magnitudes of each loss mechanism shown in Fig.7 results in the optimal design point shifting. Figure 8 shows how each design parameter, and the resulting efficiency, changes when finding the optimum design for each number of stages. Solid lines show the first stage and dashed show the last. Some parameters remain almost constant across the designs. For every number of stages the last stage does 10% more work than the first, as seen from the grey line. Gas density is higher in earlier stages, so they have shorter blades and thus more shroud loss. The optimum point seeks to unload these lossier stages to spread entropy generation evenly across the turbine. ϕ, shown by the blue line, stays at low values of 0.25–0.28, only rising to 0.33 in the last stage of the five stage design. Λ, shown by the green line, remains at 50% as in general there is no reason to load the rotor or stator more, however reaction does increase in later stages. This is because the rotor blades are taller than the stator blades, by around 3% in the first stage and 6% in the last, resulting in less shroud leakage over the rotor. It therefore becomes preferable to increase reaction, increasing the pressure drop over the rotor and balancing leakage between the two blade rows.

With more stages the optimum ψ decreases. The increase in shroud loss at low stage numbers seen in Fig.7(d) effectively pushes the corresponding line in Fig.7(b) up. As a result increasing ψ to bring the radius down reduces shroud loss more than it increases profile and secondary loss. The increasing spans through the turbine mean later stages benefit more from this effect. In the optimal five stage design the rotor of the last stage is twice as tall as the stator of the first stage, and as a result the last stage benefits from a 30% greater stage loading. This is the cause for the increase in ϕ through the turbine as it is required to prevent high blade turning that would be penalised by profile loss.
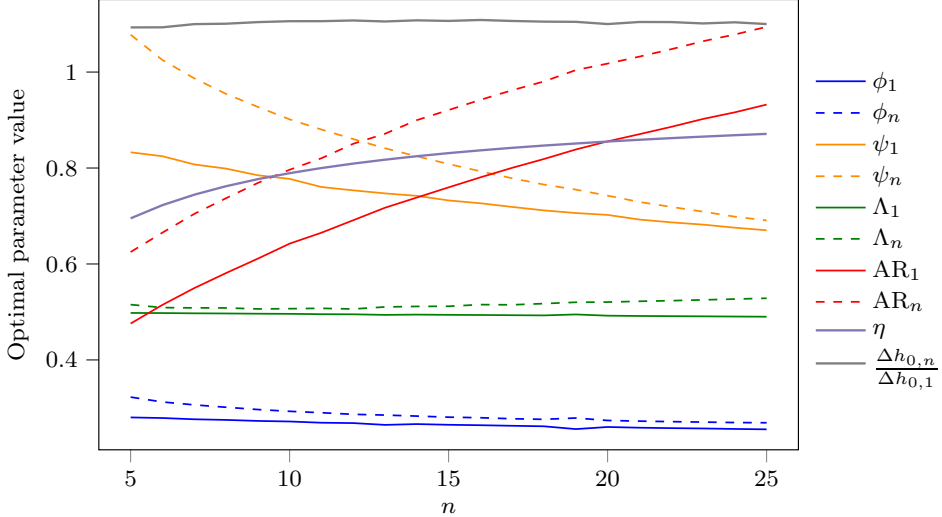
Figure 8: Turbine parameters at the optimum design point for $5 \leq n \leq 25$. Solid lines show parameters for the first stage and dashed lines show parameters for the last stage

Optimum aspect ratio increases with more stages and increases through the turbine. Figure 7(d) shows that increasing the number of stages reduces trailing edge loss, pushing the trailing edge line in Fig.7(c) down and moving its crossover point with secondary loss to the right. The tradeoff between secondary and trailing edge losses therefore begins to favour the greater secondary loss, driving the optimal AR up. The same effect causes AR to increase through the turbine as later stages have larger blades.

The net effect of each of these changes to design point is for efficiency to increase with more stages, however gains become marginal. η goes from $70\,\%$ to $80\,\%$ between five and eleven stages, but only $86\,\%$ to $87\,\%$ between twenty and twenty-five. Therefore there is a driving force to move to more stages, however a reduction in mechanical complexity can be achieved with a minimal penalty to thermodynamic performance.

The small blades seen in designs means that blade Reynolds numbers may be low enough for boundary layers to remain laminar. Equations 22 and 25 assume turbulent boundary layers and if this is not the case then laminar separations may cause more loss than predicted [22]. Figure 9(a) shows the average Reynolds number for the optimal designs for five to twenty-five stages. Re is high enough for fully turbulent boundary layers and does not change significantly across stage numbers, increasing $20\,\%$ for a $400\,\%$ increase in stage number. This is because although designs with fewer stages have smaller blades, they also have increased blade and flow velocities, keeping Re fairly flat overall.

Figure 9(b) shows the changes in the total number of blades for the optimal designs at each stage number. Like Reynolds number the change is also mostly flat, with a $20\,\%$ increase in blades between five and twenty-five stages. Although more stages means more blade rows, the reduced radii brings down the number of blades per row from 450 for five
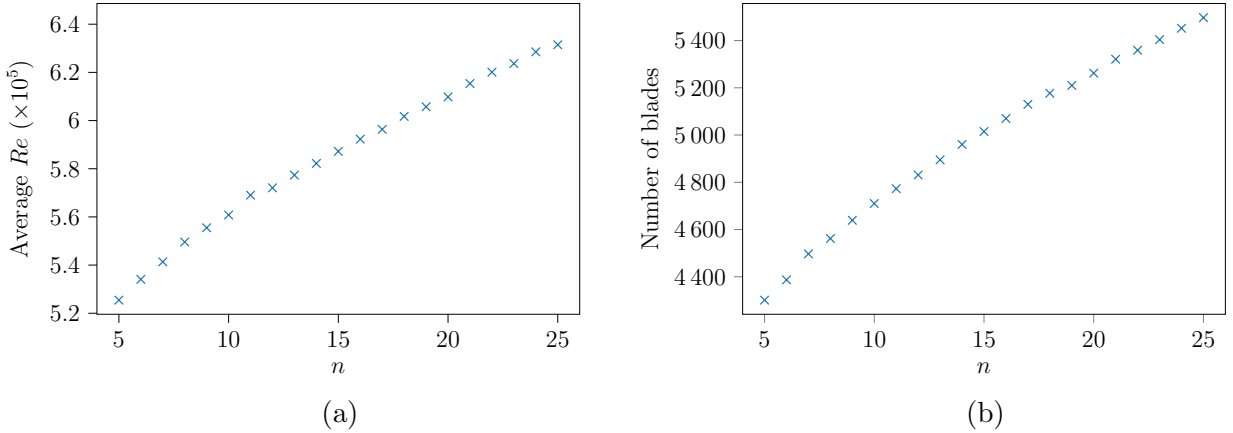
Figure 9: (a) Average Reynolds number and (b) total number of blades at the optimum design point for for $5 \leq n \leq 25$

stages to 110 for twenty-five stages. The number of blades is a major determinant in the time and cost of machining, so although having more stages will increase machining time, the penalty is not prohibitive to moving to more stages for greater efficiency.

2.3 Comparisons to a conventional aeroengine

The results of the optimisation described in section 2.2 show that the helium turbine for SABRE lies in an unconventional design space compared to most gas turbines. The high pressure (HP) turbine in a modern jet engine might operate with a ϕ of 0.6 and a ψ of 1.8 [24]. On the other hand the helium turbine is well towards the bottom left of the Smith chart with ϕ around 0.3 and ψ in the range of 0.7–1.1. By adjusting the model to include the properties of combustion gases a representative aeroengine turbine can be tested to show how its design differs from the helium turbine.

Unlike helium, hydrocarbon combustion products cannot be assumed to behave as a perfect gas through the turbine. γ, c_p and μ will change with temperature and this will affect the efficiency, so a method of modelling the changes is needed. Poferl et al. [37] give thermodynamic and transport properties for the combustion products of A-1 jet fuel with air at an air-to-fuel ratio of fifty, representative of what may be seen in an aeroengine [24]. Best fit lines for the data produce equations for γ, c_p and μ as

$$\gamma = 1.41 - 8.49T \times 10^{-5} \tag{37}$$

$$c_p = 0.22T + 951 \tag{38}$$

$$\mu = 5.9T \times 10^{-8} - 1.71T^2 \times 10^{-11} \tag{39}$$

20

These are used in the model to predict the performance of an aeroengine turbine, the design for which is from Cumpsty and Heyes [23], who undertake a low order study of the design of a high-bypass turbofan for a modern passenger aircraft. The HP turbine is used here as its constraints, taken as those at cruise conditions, most closely match those for the helium turbine. In particular the required power outputs of the two machines are very similar. Both sets of constraints are listed in table 5 for comparison.

There are several differences between the operating conditions of the helium and aeroengine HP turbines. The HP turbine has double the mass flow rate, 65 % faster rotational speed and two instead of ten stages. The higher inlet temperature and lower inlet pressure result in a halving of inlet density compared to the helium turbine, even though helium has a gas constant seven times greater than for the combustion products. The difference in gas properties also results in the HP turbine having double the pressure ratio of the helium machine for almost the same work output. The effect of these differences is that the HP turbine has a specific speed of 0.35, an order of magnitude greater than the helium turbine (0.04) which, as explained in section 1.3, changes design significantly.

Parameter	Helium turbine	'Real' HP turbine	Optimal HP turbine
$P_{0,in}$ (bar)	145	16	
$T_{0,in}$ (K)	950	1500	
$\dot{W}_{out}$ (MW)	17	15	
$\dot{m}$ (kg s^{-1})	16	32	
Ω (rpm)	6782	11 160	
n	10	2	
ϕ	0.28	0.53	0.25
ψ	0.85	2.00	0.60
Λ	0.50	0.15	0.48
AR	0.72	0.68	1.6
$\Delta h_{0,n}/\Delta h_{0,1}$	1.11	0.82	1.18
η (%)	78.9	83.0	89.0

Table 5: Comparison of parameters for an optimal 10 stage helium turbine, a 'real' HP turbine and an optimised HP turbine. Values for ϕ, ψ, Λ and AR are average values across the turbines

The constraints for the HP turbine can be applied to the optimisation routine to determine a design for peak efficiency. The parameters for this optimum, as well as those for the optimum ten stage helium turbine and the 'real' HP turbine are given in table 5 alongside the efficiency of each as predicted by the model. Both HP turbine designs are assumed to have a shroud gap of 0.2 mm and a trailing edge thickness of 1 mm, representative of tolerances in a real engine [24]. Cross sections of all three are shown in Fig.10, demonstrating the differences in radius and blade size.
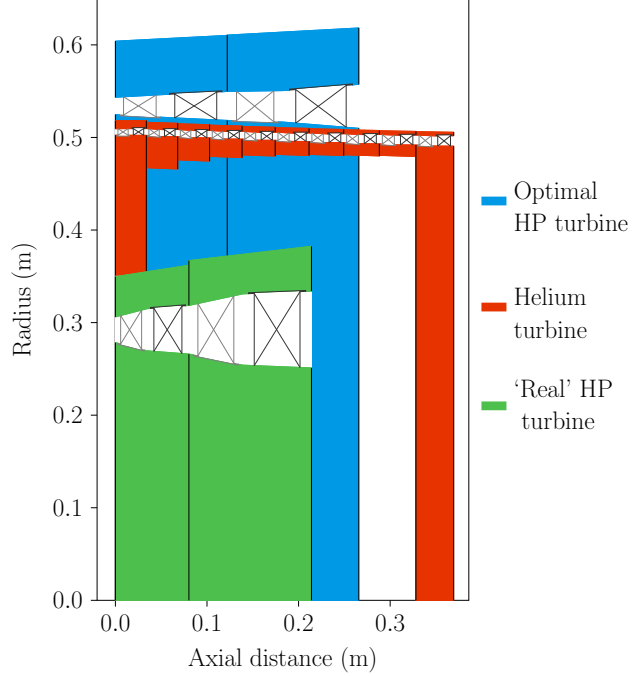
Figure 10: Meridional views of the optimal 10 stage helium turbine compared with two designs for an aeroengine HP turbine

Of most note in both table 5 and Fig.10 are the differences between the optimised and 'real' HP turbines. Similar to the helium turbine, the optimised HP turbine operates at low values of ϕ, ψ and AR, each being 30 %–50 % of those for the 'real' turbine. The effect of the low stage loading coefficient is to nearly double the mean radius to 0.53 m. The model predicts the 'real' turbine to have an efficiency of 83 %. This is lower than the 90 % suggested by Cumpsty and Heyes [23], indicating the model may be overestimating loss in this case, but compared the the 89 % efficiency predicted for the optimised design it is apparent that the 'real' design is operating away from the purely aerodynamic optimum. This is because in reality the HP turbine of an aeroengine is designed for more than just aerodynamic performance. Problems associated with cooling, stress and structural requirements must be considered. The turbine interacts with the combustion chamber and low pressure turbine, meaning that rather than the constant radius design presented here it would vary in radius between the two components [16]. Each of these additional constraints are not accounted for in this optimisation, causing the designs to differ.

Figure 11 shows a breakdown of loss mechanisms for each turbine while sweeping over the mass flow rate of the working gas. In each case all other constraints and parameters are kept constant as listed in table 5. The differences between these graphs help to explain the differences between the three designs. As seen earlier, Fig.11(a) shows that at the design point of $\dot{m} = 16\,\mathrm{kg\,s^{-1}}$ the helium turbine is dominated by shroud loss. The 'real' HP turbine in Fig.11(b) is almost the complete opposite, with profile loss being the most significant at $\dot{m} = 32\,\mathrm{kg\,s^{-1}}$, followed by trailing edge and secondary losses with shroud

22

loss coming last. This explains why the optimised HP turbine moves to a lower stage loading and a higher radius. As seen in Fig.11(c) profile and trailing edge losses are reduced without affecting other mechanisms, resulting in a more efficient design.

(a)

(b)

(c)
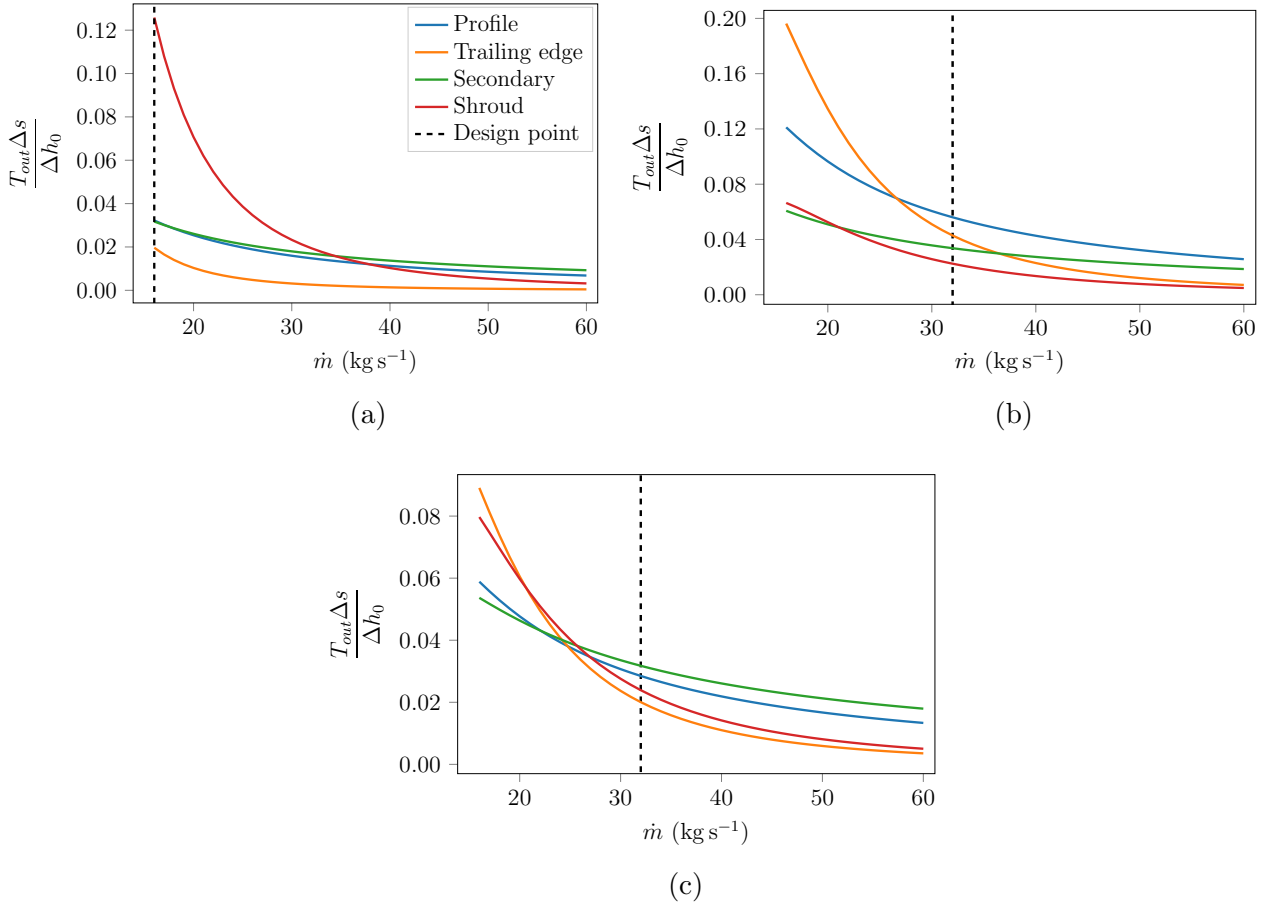
Figure 11: Loss mechanism breakdown when varying mass flow rate of working gas for (a) an optimised ten stage helium turbine (b) a 'real' aeroengine HP turbine (c) an optimised aeroengine HP turbine. All other constraints and parameters are kept constant as listed in table 5. The design mass flow rate of each turbine is shown by the vertical dashed line.

The variation in loss in the helium and aeroengine turbines can be explained by different geometry. The 1/3 narrower shroud gap and three times thicker trailing edge in the HP turbine partially explains the differences, but the main reason is the size of the blades. The 'real' HP turbine has blades as much as ten times taller with axial chords up to five times longer than those in the ten stage helium turbine. The large blade height and small shroud gap result in low shroud leakage, however the thicker trailing edge means normalised loss in the wake of the aeroengine blades is triple that in the helium turbine.

Figure 11(a) can be used to estimate how much helium would be needed in SABRE for the helium turbine to resemble an HP aeroengine turbine. Increasing mass flow has a strong effect on the shroud loss as it increases the blade spans in two ways. $\dot{m}$ appears explicitly in Eq.8 for blade span, but it also indirectly works to reduce the mean radius. More mass flow means less enthalpy drop for the same work, decreasing Δh_0 in Eq.5 and thus bringing

down the mean radius. This increase in blade size also helps to decrease trailing edge loss. By increasing the mass flow rate of helium by a factor of 3–4 it could therefore be possible to match the relative magnitudes of each loss mechanism in the helium turbine to those in an aeroengine. The problems with doing this in SABRE are explained in section 1.1 and so this analysis demonstrates why there must be significant differences between the helium turbine and more conventional designs found in aeroengines.

2.4   Sensitivity to geometric constraints

In previous sections it has been shown that the performance of the helium turbine in SABRE is constrained by both the conditions imposed on it by the cycle as a whole, and the geometric tolerances imposed on it by mechanical limits. As the cycle constraints cannot be changed, the only way to increase optimum efficiency for a given number of stages is to change the geometric constraints. The achievable tolerances will determine the minimum number of stages, and by extension the mechanical complexity, needed for a turbine with the 85 % efficiency required by REL. The sensitivity of efficiency to each constraint can be used to show which will provide the best return on the technical investment needed to achieve it.

All work so far has assumed a trailing edge thickness and shroud gap of 0.3 mm and a pitch-to-chord ratio of 1.1. The effect of the trailing edge and shroud on loss has been discussed, however the pitch-to-chord ratio has not been considered in depth. It appears in Eq.14 as a constant that determines blade spacing and throat width. As throat width appears in the denominator of both terms in Eq.26, the effect of increasing w is to decrease trailing edge loss. Increasing p/C_x will therefore reduce trailing edge loss. This increase in spacing isn't penalised in the model, even though it is well established that it has an effect on profile loss [22]. Instead it is assumed that the blades are well design by setting the value of $\Delta V/\bar{V}$ in Eq.23 to the optimum value of $1/\sqrt{3}$ and then choosing a value of p/C_x within limits for which it is known that such blades can be designed [24].

As well as changing g, t_{TE} and p/C_x there is one more change that can be added to the design. The model assumes that the shrouds on the stator and rotor blades are identical, with the stator shroud sealing against the hub just as the rotor seals against the case and both having the same contraction coefficient in Eq.18. However, as the stator blades are not rotating they are not subject to the same forces as rotor blades, for which the mass of the shroud adds a considerable centrifugal stress. It is therefore possible to create an enhanced stator shroud using cavities and labyrinth seals as seen with the stator wells of modern turbines [27], thereby cutting leakage over the stator. The proportion by which the leakage is cut is adjusted in the model to find how design is changed as a result.

Table 6 shows how the design of the turbine changes when each constraint is modified

individually, and also the result when all modifications are applied at once. The magnitudes of the modifications themselves are somewhat arbitrary, but they are based on what may be possible with current technology. Howell et al. [38] showed that high lift blading can be used to increase p/C_x to 1.5 without loss in performance. t_{TE} and g are halved to $0.15\,\mathrm{mm}$ each to reflect improved machining tolerances and vibration control, as investigated in Karimjee's project. The cut in stator shroud leakage is found by moving from a single seal on the standard shroud to ten on the enhanced stator shroud. Denton [22] suggests that shroud leakage is roughly inversely proportional to the square root of the number of seals, so it is cut by 70 % in the stator.

The results in table 6 show that some modifications have a larger effect than others when finding the minimum number of stages for 85 % efficiency. With no changes to the constraints the model predicts nineteen stages are needed. Increasing p/C_x reduces this by only one to eighteen, and halving trailing edge thickness brings it down by two. Both of these parameters affect trailing edge loss which, as seen in Fig.7(d), is the least significant mechanism with seven or more stages, making design insensitive to changes that reduce it. Design is much more sensitive to reductions in shroud loss, so halving the shroud gap reduces the stage requirement by seven and cutting stator leakage reduces it by six. Applying all of these modifications to a single design makes it possible for a seven stage turbine to reach 85 % efficiency. This indicates that REL's aim of an adequately efficient helium turbine with reduced mechanical complexity is achievable through the use of sufficiently advanced technology. There is even room for higher efficiency while maintaining fewer than half the number of stages suggested in previous work [13] [15].

Modification	n	ϕ	ψ	Λ	AR	$\frac{\Delta h_{0,n}}{\Delta h_{0,1}}$
None	19	0.26	0.73	0.51	0.92	1.11
$p/C_x = 1.5$	18	0.27	0.72	0.52	1.03	1.11
$t_{TE} = 0.15\,\mathrm{mm}$	17	0.27	0.73	0.52	1.18	1.12
$g = 0.15\,\mathrm{mm}$	12	0.27	0.73	0.52	0.71	1.10
Stator leakage cut by 70 %	13	0.31	0.75	0.35	0.76	1.13
All of the above	7	0.32	0.73	0.35	0.90	1.26
None	7	0.29	0.90	0.50	0.63	1.11

Table 6: Design points at the minimum number of stages for 85 % efficiency with changing geometric constraints. The optimal seven stage design with no modifications, which has an efficiency of 74.4 %, is included for comparison

The parameters for each design in table 6 show that the aerodynamic design point of the turbine doesn't change significantly. The dominant loss mechanism is still shroud loss, so the design point tries to mitigate it as far as possible. ϕ and ψ stay essentially constant at low values and the last stage does more work than the first for the reasons described

in section 2.2. Aspect ratio increases where trailing edge loss decreases in response to the trade off with secondary loss seen in Fig.7(c). The only as yet unseen change is to reaction. When the stator leakage is cut relative to the rotor it is preferable to reduce the pressure drop over the rotor that drives leakage by reducing reaction. The effect of this on blade profiles in shown in Fig.12. Figure 12(a) is the optimum design for seven stages and no modifications to the geometric constraints, which has a reaction of 50 %. Figure 12(b) is the optimal seven stage design when all geometric modifications applied. The lower reaction produces low turning stator blades and more bucket-like rotor blades. Figure 12 is not to scale; the design in Fig.12(a) is 210 mm long whereas the design in 12(b) is only 105 mm, a result of the higher aspect ratio producing shorter axial chords.

(a)

(b)
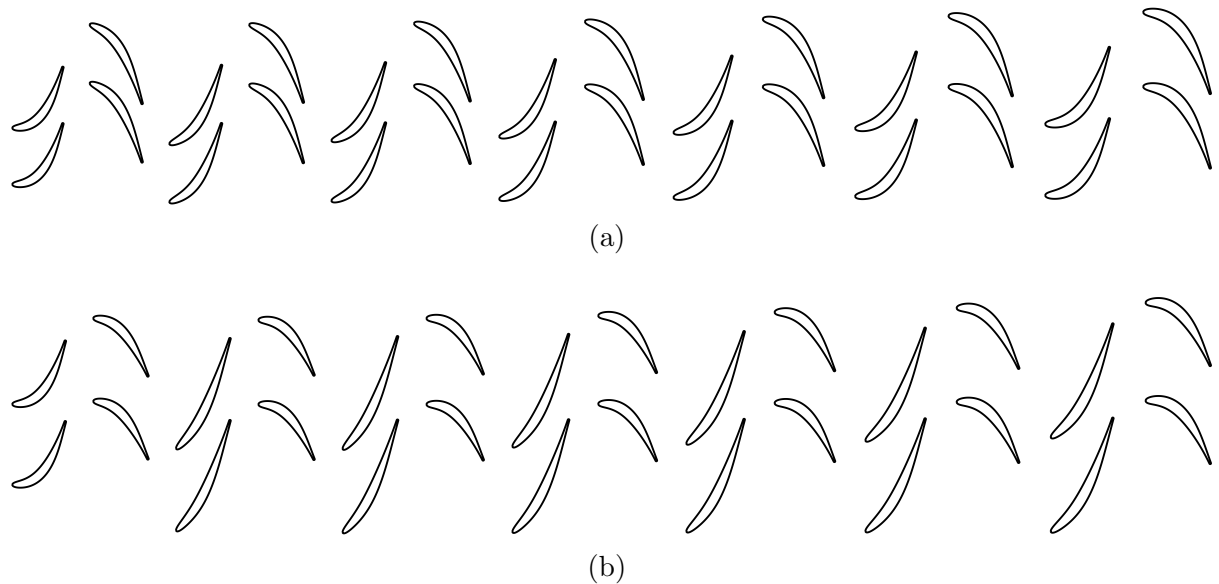
Figure 12: Blade-to-blade profiles (not to scale) for optimal seven stage designs with (a) no modifications to geometric constraints (b) modifications as listed in table 6, along with design parameters for both turbines

Aerodynamic modelling shows that the helium turbine in SABRE lies in a design space well away from that of a conventional turbine. The dominance of shroud loss forces the designer into practices not normally considered to reach efficiencies that make the cycle feasible, but adopting advanced aeromechanical technologies could allow for a more efficient and less complex machine. Communicating these findings with engineers at REL it has revealed that their own modelling has come to similar conclusions, and they are now pursuing a sixteen stage helium turbine at a radius of approximately 0.6 m. They estimate an efficiency close to 80 % for this design, which is intended for use in an upcoming demonstrator engine, and are also predicting shroud leakage to be the dominant source of entropy generation. This verifies the modelling presented here, indicating that the trends predicted with correlations are likely to align with those seen in the actual machine.

3 Thermomechanical Modelling

Aerodynamic modelling has described how the helium turbine in SABRE could be designed to maximise its thermodynamic efficiency, and therefore the thermodynamic efficiency of the entire cycle. This will benefit the performance of the engine on its own, however aeroengines don't tend to operate in isolation and so it is the net performance of the engine-airframe system that is the key indicator of success. One parameter that will determine this performance is engine mass. Lifting material into space is expensive; SpaceX's Falcon 9 advertises a cost of US\$2720/kg, twenty times less than that of NASA's space shuttle [39] but still costly when lifting satellites and manned missions. SABRE is intended for SSTO vehicles that should bring the cost down further, but this can only be achieved if the engine consumes as little fuel as possible in lifting its own mass into orbit.

Aerodynamic modelling has shown the dominance of shroud loss in helium turbine designs, and a sensitivity analysis has revealed that changes to the shroud gap have a significant impact on the performance of the turbine. Transient changes to the shroud gap that arise due to the different rates of expansion of the hub and casing during operation are therefore a concern. These changes are similar to the 'hot re-slam' seen in aeroengines, which sets the limit for g to prevent the blades rubbing on the casing [40]. This section will describe the approach taken for thermomechanical modelling, which aims to predict the mass and transient expansion behaviour of a design chosen from aerodynamic modelling.

3.1 Modelling approach

To estimate turbine mass it is necessary to calculate the sizes of each component based on stress limits. This must be done in such a way that the turbine can hold up to the extremes of its operating envelope, meaning high temperatures and possible off-design operation should be accounted for.

The material considered here is Inconel 718 [41], a nickel-based superalloy commonly used in aeroengines for its excellent strength and creep properties at high temperatures [24]. Titanium and steel alloys are attractive alternatives due to their lower density and high strength, but they quickly lose this strength at the high temperatures seen in the turbine and so cannot be used [42]. The Poisson's ratio and density of Inconel 718 are

$$\nu = 0.3 \tag{40}$$

$$\rho = 8300 \, \text{kg} \, \text{m}^{-3} \tag{41}$$

27

To accurately predict component behaviour at high temperatures, the changes in material properties with temperature are also needed. The specific heat and thermal conductivity of Inconel 718 are given by

$$c_p = 400 + 0.15e^{\frac{T-300}{90}} \tag{42}$$

$$\lambda = \frac{1}{60}T + 5 \tag{43}$$

Values for ν, ρ, c_p and λ are taken from Díaz-Álvarez et al. [43], with equations for c_p and λ fit to data. The coefficient of thermal expansion is given by Lewandowski and Overfelt [44] as

$$\alpha_T = (1.28 + 5 \times 10^{-4}(T - 366)) \times 10^{-5} \tag{44}$$

and a curve fit [45] for yield stress gives

$$\sigma_y = \left(1250 - e^{\frac{T-273}{128}}\right) \times 10^6 \tag{45}$$

Finally the Young's modulus is given by Thomas et al. [46] as

$$E = 166.2(1 + \nu)\left(1 - 0.5 \times \frac{T - 300}{1673}\right) \times 10^9$$

The equations needed for stress in the hub and case will depend on how the turbine is constructed. To save mass it is assumed that the hub is a drum, as in an aeroengine compressor, with each section consisting of an integrally bladed ring that extends the length of a stage. The first and last stages are discs extending down to the shaft to enable the transfer of power, with every other ring connecting up to form a continuous closed drum. The casing is similar, with rings of integrated stator blades for each stage. Visualisations of turbines constructed in this manner can be seen in Fig.10 and Fig.14(a), and an axial cross section is shown in Fig.13 with the relevant radii labelled. The machine would be assembled by alternately stacking a hub ring and a casing ring axially.

In this analysis each ring is treated as if it is in isolation i.e. the adjacent rings are not accounted for. This is will result in conservative estimates for hub thickness as the discs at each end would provide some confining force for the drum as a whole, but analysis of this effect requires finite element modelling that is ill-suited to design space exploration. Two mechanisms act on the hub rings to produce stress: rotation and pressure. The maximum
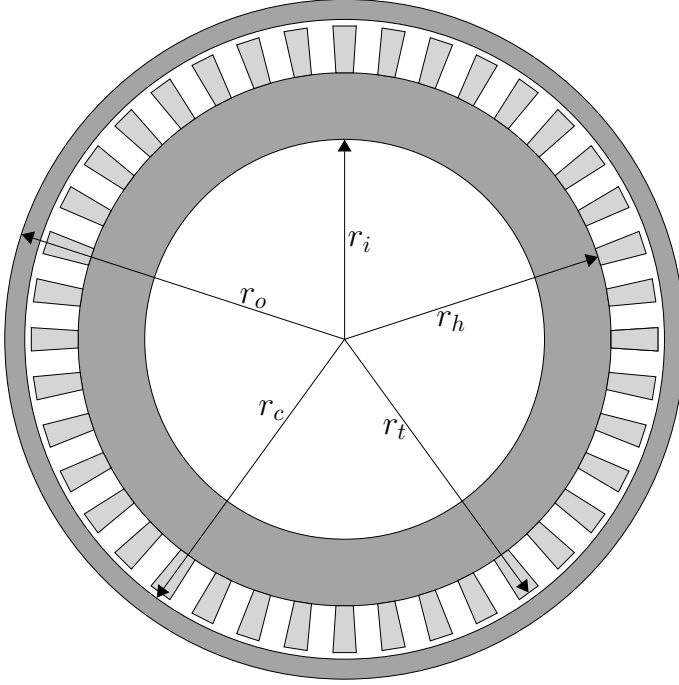
Figure 13: Axial view (not to scale) of the turbine construction, showing the thick-walled hub and case rings

stress in a ring due to rotation occurs at its inner radius and is given by Roark [47] as

$$\sigma_{max} = \frac{\rho\Omega^2}{4}\left((3+\nu)r_h^2 + (1-\nu)r_i^2\right) \tag{46}$$

and the maximum stress from pressure, also given by Roark on the inner radius of a thick-walled cylinder, is

$$\sigma_{max} = \frac{2Pr_h^2}{r_h^2 - r_i^2} \tag{47}$$

Where P is the pressure difference between the inner and outer surfaces. Atmospheric pressure is less than 1% of the helium inlet pressure of $145\,\text{bar}$, so it is neglected and P is taken to be the local helium pressure. The hub is also subject to a centrifugal stress that arises from the mass of the blades it holds. Armand [48] suggests that this can be accounted for by spreading the total force from the blades over the area of the blade row, which in this case is 1.5 times the axial chord. This results in a negative pressure that acts on the outer radius of the hub and produces a maximum stress on the inner radius in accordance with Eq.47. Using the blade root stress σ_{root}, given in Eq.55, this 'blade pressure' P_b is

$$P_b = \frac{N\sigma_{root}A_b}{2\pi r_h \times 1.5C_x} \tag{48}$$

There are two limiting stress states considered for the hub. These are pure rotation for which there is no net pressure exerted by the gas, reflecting a possible uncontrolled decompression of the helium loop or an equalisation of pressure inside the drum, and pure pressure, reflecting starting conditions where the loop is pressurised but the rotor has not started spinning. In both states the metal may be fully heated to the local gas temperature, so the change in strength of Inconel 718 must also be accounted for. The hub should be able to withstand both of these scenarios, so the inner radius is determined by the limiting condition. For pure rotation the inner radius can be found by summing Eq.46 with Eq.47, using P_b as the pressure in the latter, and applying the Tresca yield criterion. Solving the resulting fourth order polynomial for r_i gives

$$r_i = \sqrt{\frac{2\sigma_y - \rho\Omega^2 r_h^2(1+\nu) - 2\sqrt{\sigma_y^2 + \rho^2\Omega^4 r_h^4 + 2\rho\Omega^2 r_h^2(P_b(1-\nu) - \sigma_y)}}{\rho\Omega^2(1-\nu)}} \quad (49)$$

A full derivation for this can be found in appendix A.2. For the pure pressure condition the pressure is assumed to be equal to the inlet stagnation pressure. Rearranging Eq.47 for r_i gives

$$r_i = \sqrt{\frac{(\sigma_y - 2P_{01})r_h^2}{\sigma_y}} \quad (50)$$

The minimum r_i between Eqs.49 and 50 is used. In general it is found that the rotation condition is the limiting one.

The casing is only subject to stress from internal pressure, so analysis required for the outer radius is less involved. Equation 47 applies for internal pressure as well as external, and rearranging for the case outer radius gives

$$r_o = \sqrt{\frac{\sigma_y r_c^2}{\sigma_y - 2P_{01}}} \quad (51)$$

To find the transient changes in shroud gap as the turbine accelerates and heats up expressions for expansion of the hub and case radii are needed. For the hub, Roark [47] gives the change in radius due to rotation and net pressure from the blades and gas. Thermal expansion is calculated by integrating the coefficient of thermal expansion given in Eq.44 between the starting temperature, assumed to be $293\,\mathrm{K}$, and the temperature of the metal. Assuming the fractional change in radius is small, this can be multiplied by the initial hub radius to give the change. Summing the three contributions gives the overall change in hub radius as

$$\Delta r_h = \frac{\rho \Omega^2 r_h}{4E} \left((1-\nu)r_h^2 + (3+\nu)r_i^2 \right) + \frac{(P_b - P_{01})r_h}{E} \left(\frac{r_h^2 + r_i^2}{r_h^2 - r_i^2} - \nu \right) + r_h \int_{293}^{T} \alpha_T dT \quad (52)$$

The change in case radius is only due to pressure and thermal expansion, found similarly using Roark's [47] formula and integrating α_T to give

$$\Delta r_c = \frac{P_{01}r_c}{E} \left(\frac{r_o^2 + r_c^2}{r_o^2 - r_c^2} + \nu \right) + r_c \int_{293}^{T} \alpha_T dT \quad (53)$$

Blade profiles are generated in the model for aerodynamic purposes, but they can also be used to calculate the stress at the blade root. This can then be used to check for failure, and if the root is found to be at risk of yielding a thicker profile can be applied. The root stress arises due to the mass of the rotating blade and shroud. The shroud is considered to be plate at the tip of the blade with a thickness $t_{shr} = 1\,\mathrm{mm}$, which is reasonable for a turbine of this size [49]. The shroud spans one blade pitch at the tip, which is a linear function of the midspan pitch defined by the pitch-to-chord ratio, and extends an eighth of an axial chord up and down stream of the blade. The mass of the shroud is therefore

$$m_{shr} = \frac{5}{4} C_x t_{shr} \times C_x \left(\frac{p}{C_x} \right) \frac{r_t}{r_m} \times \rho \quad (54)$$

With this, the root stress is

$$\sigma_{root} = \frac{\rho \Omega^2}{2} \left(r_t^2 - r_h^2 \right) + \frac{m_{shr} r_t \Omega^2}{A_b} \quad (55)$$

This does not account for bending forces on the blades due to the gas, as this is assumed to be small compared to centrifugal forces. The elongation of the blade due to rotation and thermal expansion can also be found

$$\Delta b = \frac{\rho r_t^2 \Omega^2}{2E} \left[\frac{2r_t}{3} - r_h + \frac{r_h^3}{3r_t^2} \right] + \frac{m_{shr} r_t \Omega^2}{E A_b} (r_t - r_h) + b \int_{293}^{T} \alpha_T dT \quad (56)$$

Derivations for both of these are given in appendix A.3. The change in the shroud gap as a result of rotation, pressurisation and thermal expansion can now be found as the difference between the change in case radius and the changes in hub radius and blade span, giving

$$\Delta g = \Delta r_c - (\Delta r_h + \Delta b) \tag{57}$$

With all dimensions determined, turbine mass can be calculated. Each ring for the hub and casing is of constant thickness and extends the length of the stage, so their masses are

$$m_h = 2\pi\rho(r_h^2 - r_i^2) \times 1.5(C_{x,12} + C_{x,23}) \tag{58}$$

$$m_c = 2\pi\rho(r_o^2 - r_c^2) \times 1.5(C_{x,12} + C_{x,23}) \tag{59}$$

Blade mass is found as the mass of a single blade multiplied by the number of blades in the row like so

$$m_b = \rho b A_b N \tag{60}$$

The total mass of the turbine is therefore

$$m_{turbine} = \sum_n m_h + m_c + m_b + m_{shr} \tag{61}$$

Transient analysis of thermal expansion requires a method to estimate heat transfer from the helium to the hub and case. For the purposes of this low order model several assumptions are made to simplify the problem. Heat transfer to blades is ignored as it can be assumed that, because the rotor and stator have almost the same number of blades, they have the same thermal mass and heat transfer through them to the rings is approximately equal for both the hub and case. All heat transfer is calculated through the endwalls, which are considered to be flat plates with fully turbulent boundary layers. Incropera et al. [50] give the Nusselt number as

$$Nu_{x,m} = 0.0296 Re_{x,m}^{4/5} Pr_m^{1/3} \tag{62}$$

where $Re_{x,m}$ is defined with average gas properties and velocities across the stage like so

$$Re_{x,m} = 1.5(C_{x,12} + C_{x,23}) \times \frac{1}{3}\left(\frac{\rho_1 V_1}{\mu_1} + \frac{\rho_2 V_2}{\mu_2} + \frac{\rho_3 V_3}{\mu_3}\right) \tag{63}$$

For the hub, which is rotating, relative velocities are substituted. The Prandtl number in helium is given by Petersen [30] as

$$Pr = \frac{0.6728}{1 + P \times 2.7 \times 10^{-9}} \times \left(\frac{T}{273}\right)^{-(0.01 - P \times 1.42 \times 10^{-9})} \tag{64}$$

and Petersen also gives the conductivity of helium

$$\lambda = 0.14789 \left(\frac{T}{273.15}\right)^{0.6958} \tag{65}$$

Both of these properties are averaged across the stage in a similar manner to $Re_{x,m}$, using the static temperature at inlet, mid-stage and exit, to give Pr_m and λ_m. The stage Nusselt number is defined with the stage length, so the heat transfer coefficient is

$$h = \frac{Nu_{x,m}\lambda_m}{1.5(C_{x,12} + C_{x,23})} \tag{66}$$

A lumped heat capacity model is used for transient heat transfer. The Biot numbers found in design are well above unity, so a lumped model wouldn't generally be valid. In this case, as it is the difference between two components that is sought, it is assumed that errors will be similar in the hub and the case so the errors will offset. Ekong et al. [40] showed that a lumped model can give good agreement with finite element analysis for the transient expansion of the HP compressor drum and case in a Rolls Royce Trent 1000 engine. In the lumped model the thermal time constant for the case is

$$\tau_c = \frac{\rho c_p}{h} \left(\frac{r_o^2 - r_c^2}{2r_c}\right) \tag{67}$$

and a similar expression can be found for the hub using the relevant dimensions. ρ and c_p in Eq.67 are those of the metal, not the gas. With τ the temperature change over time from an initial temperature of $293\,\mathrm{K}$ can be found using

$$\frac{T - T_{01}}{293 - T_{01}} = e^{-t/\tau} \tag{68}$$

Details of the lumped heat capacity model can be found in Incropera et al. [50]. The transient increase in temperature is applied to the model for thermomechanical expansion by sweeping over several time constants and sampling for the temperature of the hub and case. This is then used to calculate new material properties, which along with the thermal expansion can be applied in Eqs.52, 53 and 56 to find the change in the shroud gap as the turbine warms up.

3.2 Machine mass

Using the model developed for sizing of the hub and casing it is possible to show how turbine design affects total mass. Figure 14(a) shows a meridional view of the optimal ten stage design, demonstrating the overall construction of the turbine. The discs at each end required to connect the hub to the shaft can be seen, as can the individual rings that make up the hub and case for each stage. The thickness of the hub changes significantly over the turbine, from 35 mm in the second stage to 13 mm in the ninth. This is in response to the lower temperature of the helium in later stages making the Inconel there stronger, therefore needing less material to withstand the stress from rotation.


(a)

(b)
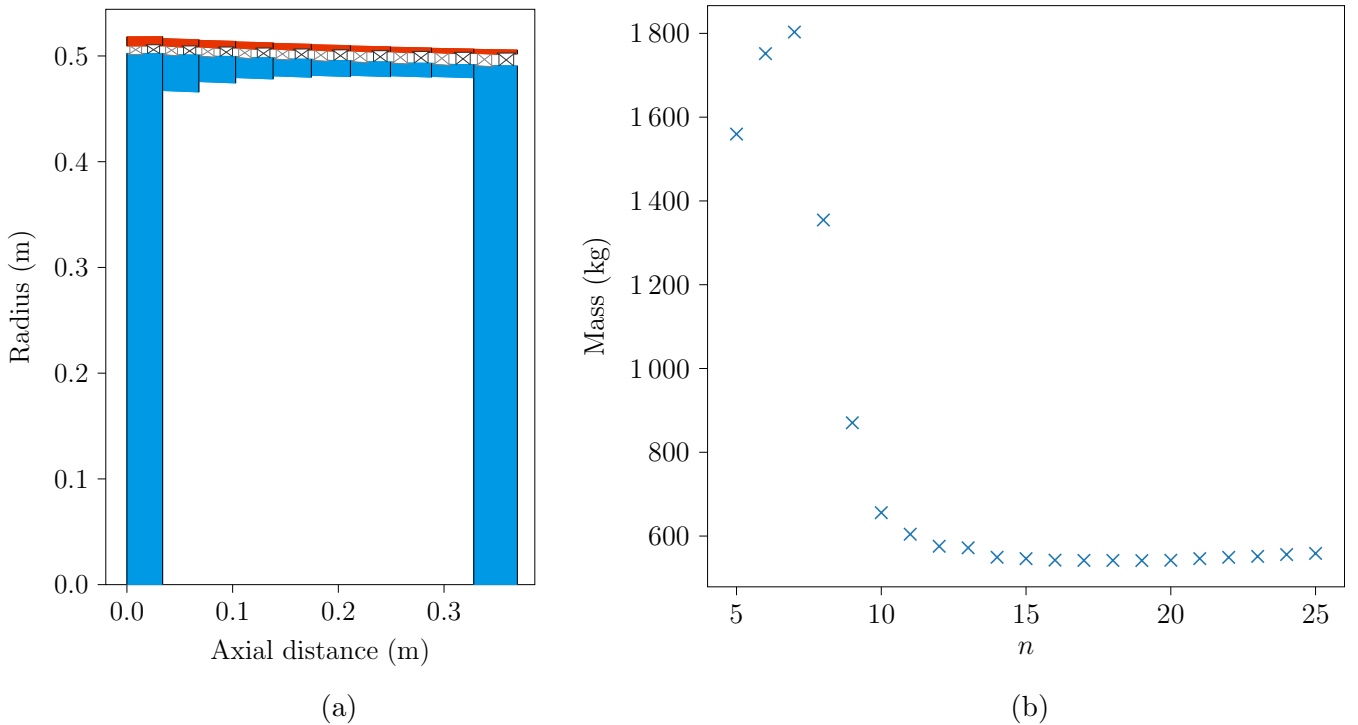
Figure 14: (a) Meridional view of the optimal ten stage design, showing the drum (blue) and casing (red) and (b) total machine mass at the optimum design point for each stage number

Figure 14(b) shows the mass of the optimal design at each number of stages. Beyond fifteen stages the line is mostly flat. This is because these designs have lower radii of around 0.4 m or less. Equation 49 shows that r_i is a strong function of r_h, so the low radius produces rings less than 1 cm thick. The total mass of the designs with fifteen or more stages is therefore dominated by the mass of the discs at each end, which are assumed to be the width of a stage. As radius is inversely proportional to the square root of the number of stages through Eq.5, moving to higher stage numbers has a diminishing effect on radius. Adding stages reduces the mass of the discs but this is offset by the mass of an extra stage. On the other hand, total mass increases sharply in designs with fewer stages. These have increasingly larger radii, resulting in much thicker hubs.

34

The five and six stage designs show a decrease in mass, however this is because the radius is so large that every hub section has become a disc, so reducing the number of stages simply removes the mass of a disc without adding mass elsewhere. What this indicates is that the model is predicting that the metal is not strong enough to support a ring of any thickness rotating at the radius, speed and temperature required by the design. Without cooling, which is not available for the helium turbine, the discs would burst at some critical temperature.

Figure 15 compares the optimal designs for five, ten and fifteen stages. The differences in hub thickness described above can be seen, with the five stage design consisting entirely of solid discs while the ten and fifteen stage turbines have rings between each end. Also evident here are the differences in radii and blade spans discussed in section 2 which contribute towards the variation in losses.
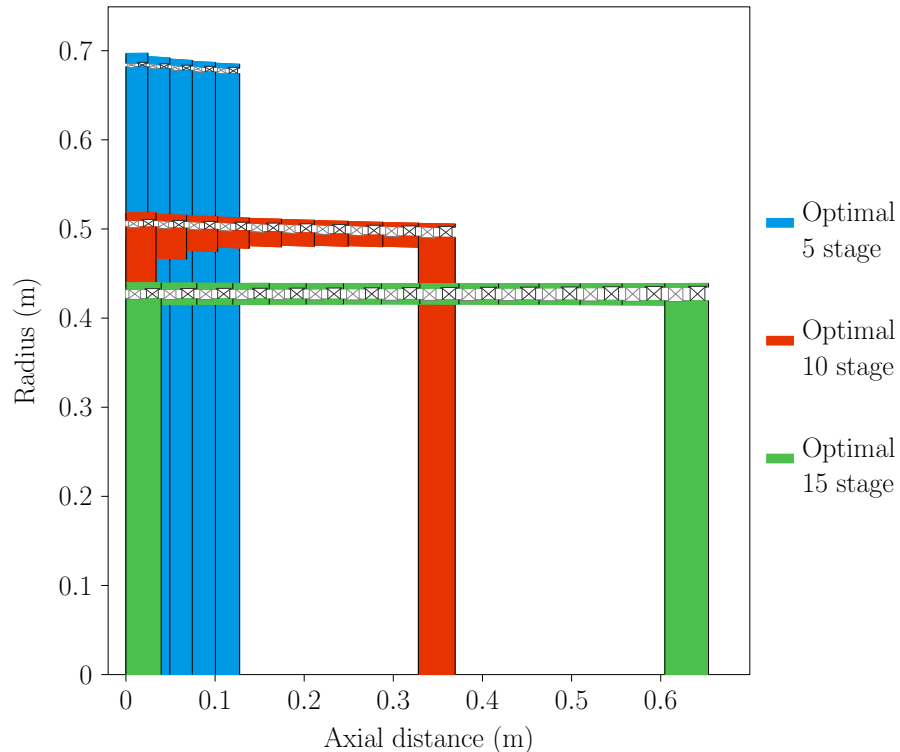

Figure 15: Meridional view of the optimal designs for five, ten and fifteen stages. The difference in drum thickness, radii and blade height can be seen between the three

These results suggest there is an additional benefit to using more stages on top of increased efficiency, however this benefit is limited. Unlike the increase in efficiency, the decrease in mass stops beyond fifteen stages. It has already been seen that the efficiency gains become more and more marginal when moving to higher stage numbers, so it appears that a good balance between mass, efficiency and mechanical complexity lies in the region between ten and fifteen stages.

3.3   Transient expansion

Transient expansion is a problem faced in aeroengines where rapid acceleration and deceleration produces significant thermal transients. Figure 16 shows results from Ekong et al.'s [40] finite element simulation of the HP compressor in Rolls Royce's Trent 1000 engine when undergoing a cycle of rapid acceleration and deceleration, known as re-slam. The lower thermal mass of the casing means it heats up and expands much faster than the drum, and the rotation of the drum results in different steady state expansions. This difference sets the maximum tip clearance for the whole operating envelope of the engine. A re-slam cycle is unlikely to be part of the requirements for the helium turbine in SABRE as any rapid changes in thrust required can be handled by the rocket engine using liquid oxygen, however thermal transients will exist during start-up of the engine that will set the maximum shroud gap. As shown in section 2 turbine performance is sensitive to this gap, so knowledge of how it changes during operation may influence design choices.
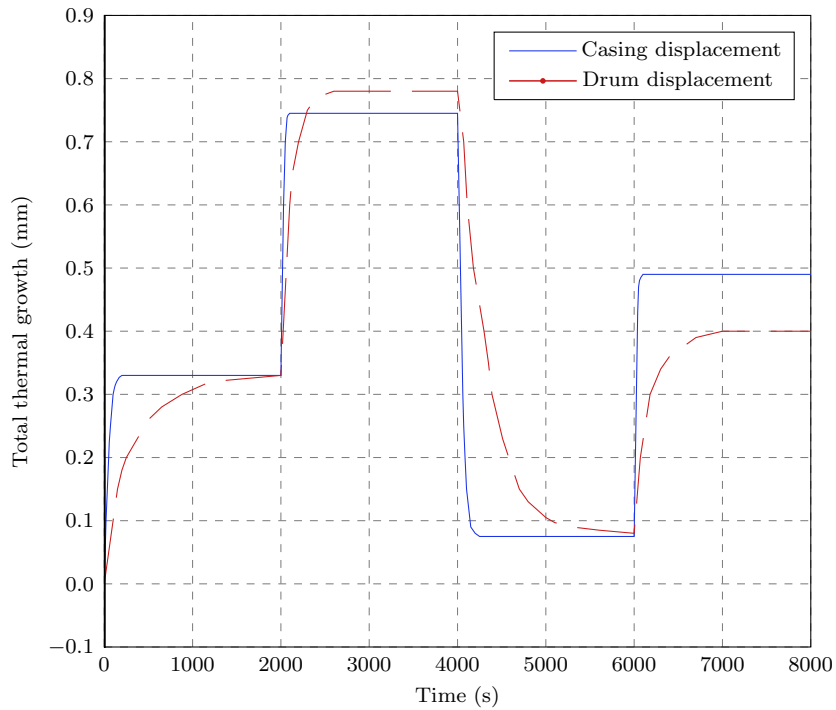

Figure 16: The variation of thermal growth of casing and drum with time over a square re-slam cycle for a single stage of the Trent 1000 HP compressor [40]

Using the transient modelling methods described in section 3.1 the change in shroud gap for the helium turbine can be plotted over time. The curve shown in Fig.17 is for the ninth stage of the optimal ten stage design. The change in the shroud gap Δg is relative to the design value, so a value of zero on the graph corresponds to a clearance of $0.3\,\text{mm}$. Labelled on Fig.17 are the four stages of the start-up procedure. The turbine starts off cold, stationary and unpressurised in the 'cold-static' condition, with the shroud gap being as machined. After full pressurisation and spin-up to the design rotational speed,
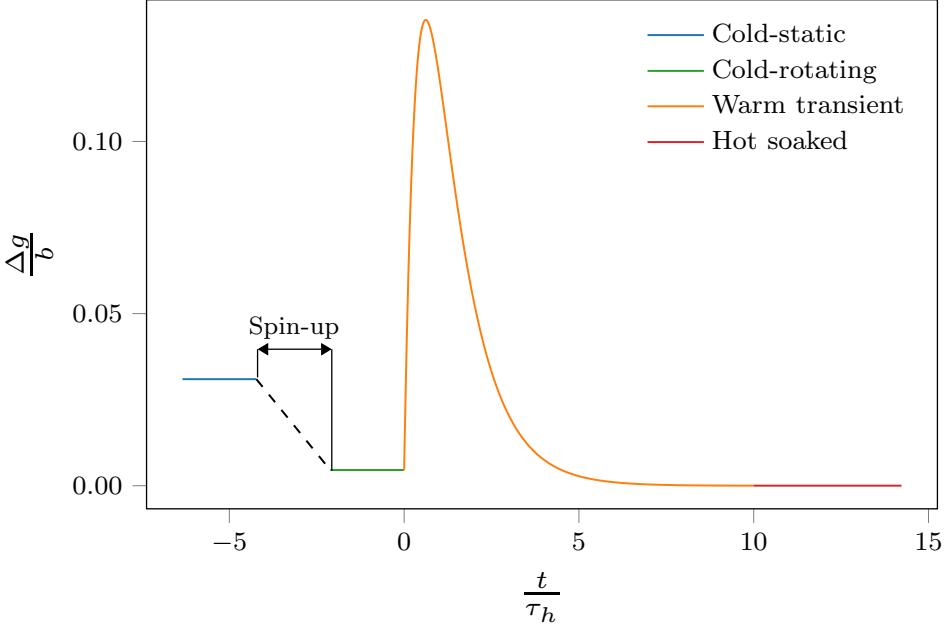
Figure 17: Transient change in shroud gap during spin-up and heating

which is shortened in the figure for the purposes of demonstration, it is assumed that the turbine is still cold and so is in the 'cold-rotating' condition. The rotation causes the hub to expand into the machined gap, closing it to less than $1\,\%$ above the design value. The turbine then starts being heated by the hot helium in the 'warm-transient' condition. This is assumed to be a step change in temperature from $293\,\mathrm{K}$ to the design operating temperature. During this phase the case, which is a third as thick as the hub and is at a larger radius, expands much faster than the hub as also seen in Fig.16. The shroud gap rapidly opens up to $13\,\%$ of the blade height, but as the hub begins to heat up the gap closes again. The final condition is 'hot-soaked', where the hub and case are fully soaked to the local helium temperature. The gap has closed to the design value due to thermal expansion of the hub and also as a result of the Inconel losing stiffness at high temperatures.

The concern with the large transient clearances seen in Fig.17 is that there may be an extended period in which the turbine operates at very low efficiency due to the leakage caused by a shroud gap more that $10\,\%$ of the blade span. Figure 18(a) shows bars of the maximum change in clearance at each start-up condition for every stage of the optimal ten stage design. These bars can be thought of as being compressed versions of the curve in Fig.17, showing how clearance changes over time. It can be seen that the first and last stages behave very differently to the others. These two stages have discs rather than rings and the resulting stiffness of the hub means it is never able to close the gap created by the expansion of the thinner case. Even when starting of with the minimum machined clearance the gap expands to over $90\,\%$ of the blade span during the 'warm-transient' phase for the first stage, and the final operating clearance of $35\,\%$ of the blade span would

result in extremely low efficiency. This behaviour can also be seen in the second and third stages, but to a much lesser extent as the thick rings in these stages are still able to expand into most of the gap left by the case. Later stages, where the hub gets thinner, show the behaviour seen in Fig.17 where there is an initial machined clearance and the hub is able to fully close the gap.
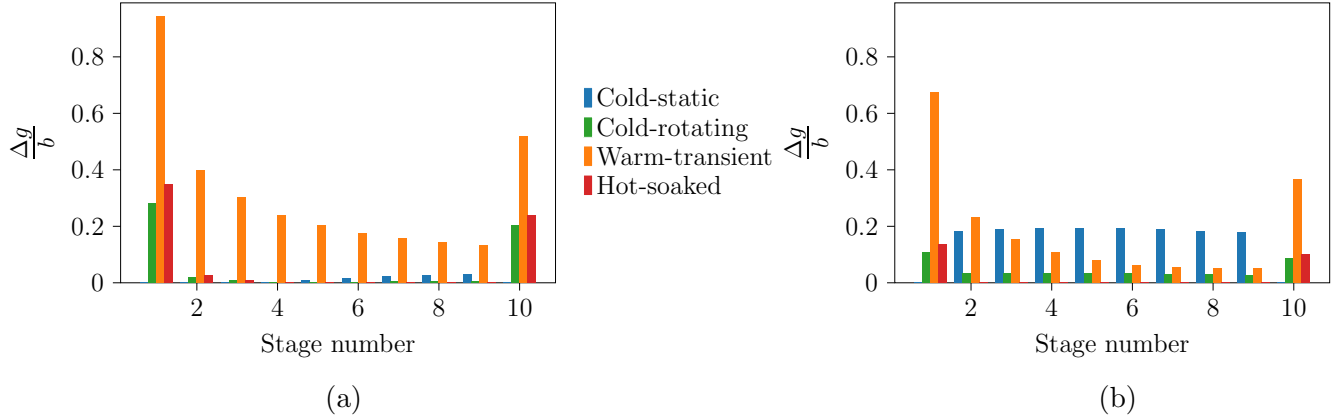

Figure 18: Transient changes in shroud gap for each stage of the optimal ten stage design with a case safety factor of (a) 1 and (b) 2

One solution to the problems seen in Fig.18(a) is to simply make the case thicker. Sizing of components has been done using a safety factor of one, but doubling this for the case will thicken it, adding thermal mass and stiffness to limit the expansion. The case makes up a small proportion of the total mass of the turbine, so doubling the safety factor only adds 8 % to machine mass. The transient behaviour of each stage with the thicker case is shown in Fig.18(b). The large transient gaps are still seen in the first and last stages, however the hub is now able to close the gap more due to the case expanding less under pressure. All of the stages in between have large gaps as machined, into which the hub is able to expand resulting in a minimum operating clearance.

Arbitrarily thickening the case is a somewhat crude method for dealing with this problem. A refined design should be able to match the expansions of the hub and case while minimising mass. Rather than making the case stiffer, the discs at each end could be made to expand more to match the case. This analysis has assumed that the discs are the width of the first and last stage, but this is not a necessity. A tapered disc would be less stiff and reduce mass while still meeting the requirement for power transfer to the shaft. Coupling this with tapered blades could further reduce the required thickness of the hub throughout the turbine.

4   Conclusions

1. The design of the helium turbine in SABRE has been explored through construction of an aerodynamic model. Design requires an axial turbine for adequate efficiency, but the low specific speed that results from constraints and gas properties pushes the turbine into an unconventional design space with hub-to-tip ratios over 0.95. As a result loss in the turbine is dominated by shroud leakage. Optimal designs are found to be those that limit leakage as much as possible, utilising low flow coefficients and balancing stage loading and aspect ratio to minimise the impact of trailing edge, profile and secondary losses.

2. Resulting turbine geometries are significantly different to those seen in conventional aeroengines. HP turbines might use two stages at a radius of 30 cm and blade spans of 5 cm–10 cm, whereas the helium turbine requires ten or more stages at a radius of 50 cm and blade spans of 0.5 cm–2 cm. These differences arise due to different working gas properties and design constraints, which for the aeroengine include cooling and component matching. When the aeroengine turbine is released from its constraints and optimised purely for aerodynamics it is found that design moves closer to the helium turbine.

3. Design is sensitive to the geometric constraints imposed by machining, vibration control and the limits of shroud and blade design. Measures to cut shroud leakage have the most impact and it has been shown that a seven stage design could achieve the required 85 % efficiency if the shroud gap and trailing edge thickness are halved, the pitch-to-chord ratio is increased to 1.5 using high lift blades and a heavier sealing arrangement is applied to the stator blades.

4. Thermomechanical modelling has revealed possible problems with transient expansion in the turbine. The requirement for discs at each end of the turbine to attach the drum to the shaft results in machine mass being dominated by the first and last stages. The difference in the thermal mass of the discs and casing result in large transient shroud gaps opening, and the stiffness of the discs prevents the hub from expanding enough to close these gaps. This could be mitigated through careful design of the hub and case, utilising a thicker case and tapered discs and blades to ensure the components match during operation.

4.1   Future work

As has been explained throughout, the constraints imposed on the helium turbine by other components in SABRE are the primary cause for the problems seen in design. Future work on the turbomachinery for SABRE may look to relax some of these constraints to

enable optimisation of a wider system within the engine. The limits on the helium inlet conditions imposed by the precooler are difficult to change without changing precooler design, however the air compressor to which the helium turbine is coupled, fixing power requirement and rotational speed, has significant scope for redesign. A new optimisation procedure could look to model the compressor in a similar manner to that presented in this project for the turbine. The rotational speed would become a floating variable, with the only constraints being the inlet conditions of the air and helium and the pressure ratio required from the compressor. The coupled optimisation would look to maximise the efficiency of the compressor-turbine system.

There is also scope to optimise the mass of the turbine. It may be that a design with reduced efficiency is preferable if it also allows for reduced mass. The exact weighting with which mass and efficiency should be optimised will depend on the sensitivity of SABRE to the performance of the helium turbine and on the aerodynamic characteristics of the airframe, such as lift-to-drag ratio, at hypersonic speeds [51]. A final design will have to account for the proper safety factors required in aeroengines [52], so any optimisation should apply them to ensure the chosen design can be realised.

Nomenclature

Greek letters		Subscripts	
Λ	Reaction	0	Stagnation quantity
Ω	Rotational speed, $\mathrm{rad\,s^{-1}}$	1	Stator inlet
Ω_s	Specific speed	2	Stator exit/rotor inlet
α	Absolute flow angle, °	3	Rotor exit
α_T	Coefficient of thermal expansion, $\mathrm{K^{-1}}$	b	Blade
		$root$	Blade root
β	Relative flow angle, °	shr	Shroud
γ	Ratio of specific heat capacities	TE	Trailing edge
δ^*	Displacement boundary layer thickness, m	c	Casing
		h	Hub
ζ_s	Entropy loss coefficient	i	Inner hub
η	Total-to-total isentropic efficiency	in	Turbine inlet
θ	Momentum boundary layer thickness, m	m	Mean
		max	Maximum
λ	Thermal conductivity, $\mathrm{W\,m^{-1}\,K^{-1}}$	n	Last stage parameter
μ	Dynamic viscosity, $\mathrm{Pa\,s}$	o	Outer casing
ν	Poisson's ratio	out	Turbine exit
ρ	Density, $\mathrm{kg\,m^{-3}}$	pro	Profile
σ	Stress, Pa	sec	Secondary
σ_y	Yield stress, Pa	t	Tip
τ	Thermal time constant, s	x	Axial
ϕ	Flow coefficient	θ	Tangential
ψ	Stage loading coefficient		

References

[1] Hempsell, M., 2013, "Progress on Skylon and SABRE," Proc. Int. Astronaut. Congr., **11**, pp. 8427–8440.

[2] Jivraj, F., Varvill, R., Bond, A., and Paniagua, G., 2007, "The Scimitar precooled Mach 5 engine," In 2nd European Conference for Aerospace Sciences.

[3] Bond, A. and Varvill, R., 2018, "Engine comprising a rocket combustion chamber and a heat exchanger," July 3rd, US Patent 10,012,177.

[4] Varvill, R., 2010, "Heat exchanger development at Reaction Engines Ltd." Acta Astronaut., **66**(9-10), pp. 1468–1474.

[5] Burns, B. R. A., 1990, "HOTOL space transport for the twenty-first century," Proc. Inst. Mech. Eng. Part G: J. Aerosp. Eng., **204**(2), pp. 101–110.

[6] Zhang, J., Wang, Z., and Li, Q., 2017, "Thermodynamic efficiency analysis and cycle optimization of deeply precooled combined cycle engine in the air-breathing mode," Acta Astronaut., **138**, pp. 394–406.

[7] Fernández-Villacé, V. and Paniagua, G., 2010, "Simulation of a combined cycle for high speed propulsion," In 48th AIAA Aerospace Sciences Meeting Including the New Horizons Forum and Aerospace Exposition, Paper No. AIAA 2010-1125.

[8] Arp, V. D., McCarty, R. D., and Friend, D. G., 1998, "Thermophysical Properties of Helium-4 from 0.8 to 1500 K with Pressures to 2000 MPa," National Institute of Standards and Technology, Tech. Note 1334 (revised).

[9] No, H. C., Kim, J. H., and Kim, H. M., 2007, "A review of helium gas turbine technology for high-temperature gas-cooled reactors," Nucl. Eng. Technol., **39**(1), pp. 21–30.

[10] Van den Braembussche, R. A., Brouckaert, J. F., Paniagua, G., and Briottet, L., 2008, "Design and optimization of a multistage turbine for helium cooled reactor," Nucl. Eng. Des., **238**(11), pp. 3136–3144.

[11] Paniagua, G., Szokol, S., Kato, H., Manzini, G., and Varvill, R., 2008, "Contrarotating turbine aerodesign for an advanced hypersonic propulsion system," J. Propuls. Power, **24**(6), pp. 1269–1277.

[12] Waldren, J. J., Clark, C. J., Grimshaw, S. D., and Pullan, G., 2019, "Non-dimensional parameters for comparing conventional and counter-rotating turbomachines," In ASME Turbo Expo: Turbomachinery Technical Conference and Exposition, Paper No. GT 2019-91632.

[13] Desai, S., 2018, "Helium Turbine Preliminary Modelling," UROP, University of Cambridge, Cambridge, UK.

[14] Clark, N., 2019, "Multi-Stage Counter Rotating Turbines for Rocket Engines," 4th year project, University of Cambridge, Cambridge, UK.

[15] Davis, W. F., 2019, "Aerodynamic Design of Helium Turbines for Rocket Engines," UROP, University of Cambridge, Cambridge, UK.

[16] Dixon, S. L. and Hall, C. A., 2013, *Fluid Mechanics and Thermodynamics of Turbomachinery*, 7th ed., Butterworth-Heinemann, Oxford, UK.

[17] Csanady, G. T., 1964, *Theory of Turbomachines*, McGraw-Hill, New York, USA.

[18] Cambridge University Engineering Department, 2009, "Compressible Flow Data Book," Cambridge, UK.

[19] Nishi, Y., Fushimi, H., Shimomura, K., and Hasegawa, T., 2018, "Performance and internal flow of a dental air turbine handpiece," Int. J. Rotating Mach., **2018**, pp. 1826489.

[20] He, T., Xia, C., Zhao, Y., Li, L., and Shu, P., 2009, "An experimental study on energy recovery by a Pelton-type expander in a domestic refrigeration system," HVAC & R Res., **15**(4), pp. 785–799.

[21] Wood, H. J., 1963, "Current technology of radial-inflow turbines for compressible fluids," ASME J. Eng. for Power, **85**(1), pp. 72–83.

[22] Denton, J. D., 1993, "Loss mechanisms in turbomachines," ASME J. Turbomach., **115**(4), pp. 621–656.

[23] Cumpsty, N. and Heyes, A., 2015, *Jet Propulsion*, 3rd ed., Cambridge University Press, Cambridge, UK.

[24] Saravanamuttoo, H. I. H., Rogers, G. F. C., Cohen, H., and Straznicky, P. V., 2009, *Gas Turbine Theory*, 6th ed., Prentice Hall, Harlow, UK.

[25] Zweifel, O., 1945, "The spacing of turbo-machine blading, especially with large angular deflection," Brown Boveri Rev., **32**(12), pp. 436–444.

[26] Yoon, S., Curtis, E., Denton, J. D., and Longley, J. P., 2014, "The effect of clearance on shrouded and unshrouded turbines at two levels of reaction," ASME J. Turbomach., **136**(2), pp. 021013–021013–9.

[27] Sultanian, B. K., 2018, *Gas Turbines: Internal Flow Systems Modeling*, Cambridge University Press, Cambridge, UK.

[28] Vázquez, R., Cadrecha, D., and Torre, D., 2003, "High stage loading low pressure turbines: a new proposal for an efficiency chart," In ASME Turbo Expo: Power for Land, Sea, and Air, Paper No. GT 2003-38374.

[29] Kulfan, B. M., 2008, "Universal parametric geometry representation method," J. Aircr., **45**(1), pp. 142–158.

[30] Petersen, H., 1970, "The properties of helium: density, specific heats, viscosity, and thermal conductivity at pressures from 1 to 100 bar and from room temperature to about 1800 K," Risø National Laboratory, Risø Rep. 224.

[31] Schlichting, H., 1979, *Boundary-layer theory*, 7th ed., McGraw-Hill, New York, USA.

[32] Dunham, J. and Came, P. M., 1970, "Improvements to the Ainley-Mathieson method of turbine performance prediction," ASME J. Eng. for Power, **92**(3), pp. 252–256.

[33] Ainley, D. G. and Mathieson, G. C., 1951, "A method of performance estimation for axial-flow turbines," ARC, R & M 2974.

[34] Denton, J. D. and Miller, R. J., 2012, "Cambridge Turbomachinery Course," Vol. 1, Lecture notes, University of Cambridge, Cambridge, UK.

[35] Nocedal, J. and Wright, S. J., 2006, *Numerical Optimization*, 2nd ed., Springer, New York, USA.

[36] Moore, J. and Tilton, J. S., 1988, "Tip leakage flow in a linear turbine cascade," ASME J. Turbomach., **110**(1), pp. 18–26.

[37] Poferl, D. J., Svehla, R. A., and Lewandowski, K., 1969, "Thermodynamic and transport properties of air and the combustion products of natural gas and of ASTM-A-1 fuel with air," National Aeronautics and Space Administration, Tech. Note 5452.

[38] Howell, R. J., Ramesh, O. N., Hodson, H. P., Harvey, N. W., and Schulte, V., 2001, "High lift and aft-loaded profiles for low-pressure turbines," ASME J. Turbomach., **123**(2), pp. 181–188.

[39] Jones, H. W., 2018, "The recent large reduction in space launch cost," In 48th International Conference on Environmental Systems, Paper No. ICES-2018-81.

[40] Ekong, G. I., Long, C. A., and Childs, P., 2013, "The effect of heat transfer coefficient increase on tip clearance control in HP compressors in gas turbine engine," In ASME 2013 International Mechanical Engineering Congress and Exposition, Paper No. IMECE 2013-64958.

[41] Eiselstein, H. L., 1962, "Age-hardenable nickel alloy," July 24th, US Patent 3,046,108.

[42] Leyens, C. and Peters, M., 2003, *Titanium and Titanium Alloys: Fundamentals and Applications*, Wiley, Hoboken, USA.

[43] Díaz-Álvarez, J., Tapetado, A., Vázquez, C., and Miguélez, H., 2017, "Temperature measurement and numerical prediction in machining Inconel 718," Sensors, **17**(7), pp. 1531.

[44] Lewandowski, M. S. and Overfelt, R. A., 1999, "High temperature deformation behavior of solid and semi-solid alloy 718," Acta Materialia, **47**(18), pp. 4695–4710.

[45] Woo, W. S. and Lee, C. M., 2019, "Innovative use of multi-heat sources for improvement of tool life in thermally assisted machining of high-strength material," J. Manuf. Process., **38**, pp. 30–37.

[46] Thomas, A., El-Wahabi, M., Cabrera, J., and Prado, J., 2006, "High temperature deformation of Inconel 718," J. Mater. Process. Technol., **177**(1-3), pp. 469–472.

[47] Roark, R. J. and Young, W. C., 1989, *Roark's Formulas for Stress and Strain*, 6th ed., McGraw-Hill, New York, USA.

[48] Armand, S. C., 1995, "Structural optimization methodology for rotating disks of aircraft engines," National Aeronautics and Space Administration, Tech. Mem. 4693.

[49] Rosic, B., Denton, J. D., and Curtis, E. M., 2008, "The influence of shroud and cavity geometry on turbine performance: an experimental and computational study—part I: shroud geometry," ASME J. Turbomach., **130**(4), pp. 334–341.

[50] Incropera, F. P., DeWitt, D. P., Bergman, T. L., , and Lavine, A. S., 2007, *Fundamentals of Heat and Mass Transfer*, 6th ed., Wiley, Hoboken, USA.

[51] Mehta, U. B., Aftosmis, M. J., Bowles, J. V., and Pandya, S. A., 2015, "Skylon aerodynamics and SABRE plumes," In 20th AIAA International Space Planes and Hypersonic Systems and Technologies Conference, Paper No. AIAA 2015-3605.

[52] Roe, R. R., 2008, "Structural design and test factors of safety for spaceflight hardware," National Aeronautics and Space Administration, NASA Tech. Standard NASA-STD-5001B.

Appendix A: Derivations

A.1 Rotor exit angle

To find α_3 for a non-repeating stage where $\alpha_3 \neq \alpha_1$ first start with the definition of the stage loading coefficient

$$\psi = \frac{\Delta h_0}{U^2} \tag{69a}$$

$$= \frac{UV_x(\tan\alpha_2 - \tan\alpha_3)}{U^2} \tag{69b}$$

$$= \phi(\tan\alpha_2 - \tan\alpha_3) \tag{69c}$$

therefore

$$\tan\alpha_2 = \tan\alpha_3 + \frac{\psi}{\phi} \tag{70}$$

The static enthalpy drop in the rotor can be found with

$$\Delta h_{rotor} = \Delta h_{02} - \frac{1}{2}V_2^2 - \Delta h_{03} + \frac{1}{2}V_3^2 \tag{71a}$$

$$= U^2\psi - \frac{1}{2}(V_{\theta2}^2 + V_{x2}^2 - V_{\theta3}^2 - V_{x3}^2) \tag{71b}$$

$$= U^2\psi - \frac{1}{2}V_x^2(\tan^2\alpha_2 - \tan^2\alpha_3) \tag{71c}$$

The static enthalpy drop for the whole stage can be found in a similar manner. This step is where the derivation diverges from those usually given for repeating stages [24], which set $V_3 = V_1$, so the enthalpy drop is

$$\Delta h_{stage} = \Delta h_{01} - \frac{1}{2}V_1^2 - \Delta h_{03} + \frac{1}{2}V_3^2 \tag{72a}$$

$$= U^2\psi - \frac{1}{2}(V_{\theta1}^2 + V_{x1}^2 - V_{\theta3}^2 - V_{x3}^2) \tag{72b}$$

$$= U^2\psi - \frac{1}{2}V_x^2(\tan^2\alpha_1 - \tan^2\alpha_3) \tag{72c}$$

Stage reaction is then defined as

$$\Lambda = \frac{\Delta h_{rotor}}{\Delta h_{stage}} \tag{73a}$$

$$= \frac{U^2\psi - \frac{1}{2}V_x^2(\tan^2\alpha_2 - \tan^2\alpha_3)}{U^2\psi - \frac{1}{2}V_x^2(\tan^2\alpha_1 - \tan^2\alpha_3)} \tag{73b}$$

$$= \frac{2\psi - \phi^2(\tan^2\alpha_2 - \tan^2\alpha_3)}{2\psi - \phi^2(\tan^2\alpha_1 - \tan^2\alpha_3)} \tag{73c}$$

Subbing in α_2 from Eq.70 and simplifying

$$\Lambda = \frac{2\psi - \phi^2((\tan\alpha_3 + \psi/\phi)^2 - \tan^2\alpha_3)}{2\psi - \phi^2(\tan^2\alpha_1 - \tan^2\alpha_3)} \tag{74a}$$

$$= \frac{2\psi - \phi^2(\tan^2\alpha_3 + 2(\psi/\phi)\tan\alpha_3 + (\psi/\phi)^2 - \tan^2\alpha_3)}{2\psi - \phi^2(\tan^2\alpha_1 - \tan^2\alpha_3)} \tag{74b}$$

$$= \frac{2\psi - 2\phi\psi\tan\alpha_3 - \psi^2}{2\psi - \phi^2(\tan^2\alpha_1 - \tan^2\alpha_3)} \tag{74c}$$

Rearranging Eq.74c results in a quadratic equation in $\tan\alpha_3$

$$\phi^2\Lambda\tan^2\alpha_3 + 2\phi\psi\tan\alpha_3 + 2\psi\Lambda - \phi^2\Lambda\tan^2\alpha_1 - 2\psi + \psi^2 = 0 \tag{75}$$

This can be solved to give the solution for α_3, taking the positive root of the quadratic to avoid non-physical solutions

$$\tan\alpha_3 = \frac{-2\phi\psi + \sqrt{(2\phi\psi)^2 - 4\phi^2\Lambda(2\psi\Lambda - \phi^2\Lambda\tan^2\alpha_1 - 2\psi + \psi^2)}}{2\phi^2\Lambda} \tag{76a}$$

$$\alpha_3 = \tan^{-1}\left(\frac{-2\psi + \sqrt{4\psi^2 - 4\Lambda(2\psi\Lambda - \phi^2\Lambda\tan^2\alpha_1 - 2\psi + \psi^2)}}{2\phi\Lambda}\right) \tag{76b}$$

A.2 Hub inner radius

At the limiting condition of purely rotational forces due to the mass of the drum and blades, the stress at the inner radius is equal to the yield stress. It is given by the sum of Eqs.46 and 47 as

$$\frac{\rho\Omega^2}{4}\left((3 + \nu)r_h^2 + (1 - \nu)r_i^2\right) + \frac{2P_b r_h^2}{r_h^2 - r_i^2} = \sigma_y \tag{77}$$

where P_b is defined in Eq.48. Multiplying through by $r_h^2 - r_i^2$ and rearranging results in a quadratic equation in r_i^2

$$\rho\Omega^2(1-\nu)r_i^4 + 2(\rho\Omega^2(1+\nu)r_h^2 - 2\sigma_y)r_i^2 - \rho\Omega^2(3+\nu)r_h^4 + 4(\sigma_y - 2P_b)r_h^2 = 0 \quad (78)$$

Solving and simplifying for r_i, taking the negative root in the quadratic equation to avoid non-physical solutions, gives

$$r_i = \sqrt{\frac{2\sigma_y - \rho\Omega^2 r_h^2(1+\nu) - 2\sqrt{\sigma_y^2 + \rho^2\Omega^4 r_h^4 + 2\rho\Omega^2 r_h^2(P_b(1-\nu) - \sigma_y)}}{\rho\Omega^2(1-\nu)}} \quad (79)$$

A.3 Blade stress and elongation

Blade root stress is equal to the sum of the stresses from the mass of the blade, which rotates at a mean radius $r_m = \frac{1}{2}(r_t + r_h)$, and the mass of the shroud, rotating at r_t. Root stress is therefore

$$\sigma_{root} = \frac{\Omega^2\rho A_b b r_m}{A_b} + \frac{m_{shr}r_t\Omega^2}{A_b} \quad (80a)$$

$$= \frac{\Omega^2\rho}{2}(r_t - r_h)(r_t + r_h) + \frac{m_{shr}r_t\Omega^2}{A_b} \quad (80b)$$

$$= \frac{\Omega^2\rho}{2}(r_t^2 - r_h^2) + \frac{m_{shr}r_t\Omega^2}{A_b} \quad (80c)$$

Stress in the blade varies along the span, so the stress must be integrated to find blade elongation

$$\Delta b = \int_{r_h}^{r_t} \frac{\sigma}{E}dr \quad (81a)$$

$$= \int_{r_h}^{r_t} \frac{\rho\Omega^2}{2E}\left(r_t^2 - r^2\right) + \frac{m_{shr}r_t\Omega^2}{EA_b}dr \quad (81b)$$

$$= \frac{\rho r_t^2\Omega^2}{2E}\left[r - \frac{r^3}{3r_t^2}\right]_{r_h}^{r_t} + \frac{m_{shr}r_t\Omega^2}{EA_b}[r]_{r_h}^{r_t} \quad (81c)$$

$$= \frac{\rho r_t^2\Omega^2}{2E}\left[r_t - r_h - \frac{r_t^3}{3r_t^2} + \frac{r_h^3}{3r_t^2}\right] + \frac{m_{shr}r_t\Omega^2}{EA_b}(r_t - r_h) \quad (81d)$$

$$= \frac{\rho r_t^2\Omega^2}{2E}\left[\frac{2r_t}{3} - r_h + \frac{r_h^3}{3r_t^2}\right] + \frac{m_{shr}r_t\Omega^2}{EA_b}(r_t - r_h) \quad (81e)$$

49

Appendix B: Risk Assessment Retrospective

The risk assessment performed at the outset of this project highlighted risks associated with desk and computer work including back pain due to poor posture, arm and hand injuries from repetitive use of a mouse and keyboard and eye strain from prolonged screen time. The dangers of faulty or damaged electrical equipment were identified. This accurately reflected the hazards encountered throughout and the recommendation to take regular breaks and take care when using computers comprehensively covered these hazards. No changes would be made to the assessment if it were to be repeated.

Appendix C: COVID-19 Disruption

Prior to the disruption caused by the COVID-19 pandemic the project plan included undertaking a CFD study to verify the low order modelling. This would have involved multi-stage simulations of the optimal five, ten, fifteen and twenty stage designs chosen by the model. Comparisons of efficiency and loss mechanisms between designs could then be made. Work completed by the end of Lent term had resulted in mesh generation for a single stage, including a basic shroud, and preliminary CFD runs to check the mesh. Plans to scale up the mesh generation procedure in AutoGrid5 to automatically produce a complete multi-stage mesh from geometry files could not be completed due to the necessary computing resources being inaccessible. The proceeding CFD simulations could therefore not be done. Results from preliminary runs are not presented in this report as the partial completion of the study means no meaningful conclusions can be drawn from them. The content of this report is not otherwise affected by the omission of the CFD and the modelling work is presented as a standalone study.